

Rest-frame far-ultraviolet to far-infrared view of Lyman break galaxies at $z \sim 3$: Templates and Dust attenuation

J. Álvarez-Márquez^{1,2}, D. Burgarella², V. Buat², O. Ilbert², and P. G. Pérez-González¹

¹ Centro de Astrobiología (CSIC-INTA), Carretera de Ajalvir, 28850 Torrejón de Ardoz, Madrid, Spain
e-mail: javier.alvarez@cab.inta-csic.es

² Aix-Marseille Université, CNRS, LAM (Laboratoire d'Astrophysique de Marseille) UMR7326, 13388, France
Descargar

Received ; accepted

ABSTRACT

Aims. This work explores, from a statistical point of view, the rest-frame far-ultraviolet (FUV) to far-infrared (FIR) emission of a population of Lyman-break galaxies (LBGs) at $z \sim 3$ that cannot be individually detected from current FIR observations.

Methods. We performed a stacking analysis over a sample of ~ 17000 LBGs at redshift $2.5 < z < 3.5$ in the COSMOS field. The sample is binned as a function of UV luminosity (L_{FUV}), UV continuum slope (β_{UV}), and stellar mass (M_*), and then stacked at optical (*BVRiz* bands), near-infrared (*YJHKs* bands), IRAC (3.6, 4.5, 5.6 and 8.0 μm), MIPS (24 μm), PACS (100 and 160 μm), SPIRE (250, 350, and 500 μm), and AzTEC (1.1mm) observations. We obtained 30 rest-frame FUV-to-FIR spectral energy distributions (SEDs) of LBGs at $z \sim 3$, and analyzed these with the CIGALE SED-fitting analysis code. We were able to derive fully consistent physical parameters, that is, M_* , β_{UV} , L_{FUV} , L_{IR} , A_{FUV} , star formation rate, and the slope of the dust attenuation law; we built a semiempirical library of 30 rest-frame FUV-to-FIR stacked LBG SEDs as functions of L_{FUV} , β_{UV} , and M_* .

Results. We used the so-called IR-excess ($\text{IRX} \equiv L_{\text{IR}}/L_{\text{FUV}}$) to investigate the dust attenuation as a function of β_{UV} and M_* . Our LBGs, averaged as a function of β_{UV} , follow the well-known IRX- β_{UV} calibration of local starburst galaxies. Stacks as a function of M_* follow the IRX- M_* relationship presented in the literature at high M_* ($\log(M_* [M_\odot]) > 10$). However, a large dispersion is shown in the IRX- β_{UV} and IRX- M_* planes, in which the β_{UV} and M_* are combined to average the sample. Additionally, the SED-fitting analysis results provide a diversity of dust attenuation curve along the LBG sample, and their slopes are well correlated with M_* . Steeper dust attenuation curves than Calzetti's are favored in low stellar mass LBGs ($\log(M_* [M_\odot]) < 10.25$), while grayer dust attenuation curves are favored in high stellar mass LBGs ($\log(M_* [M_\odot]) > 10.25$). We also demonstrate that the slope of the dust attenuation curves is one of the main drivers that shapes the IRX- β_{UV} plane.

Key words. Galaxies: starburst – Ultraviolet: galaxies – Infrared: galaxies – Galaxies: high-redshift – Cosmology: early universe

1. Introduction

About 20 years ago, the *Hubble Space Telescope* (HST) allied to the 10 m class ground-based telescopes opened up a window on the first 2 Gyr of cosmic times (Madau et al. 1996). Lyman-break galaxies (LBGs) represent the largest sample of star-forming galaxies known at high redshift ($z > 2.5$) owing to the efficiency of their selection technique in deep broadband imaging survey (Lyman-break or dropout technique, Steidel et al. 1996). These galaxies have been a key population to investigate the mass assembly of galaxies during the first gigayears of the universe (Shapley et al. 2001; Somerville et al. 2001; Madau et al. 1996; Steidel et al. 1996; Giavalisco 2002; Blaizot et al. 2004; Shapley et al. 2005; Baugh et al. 2005; Verma et al. 2007; Magdis et al. 2008; Stark et al. 2009; Chapman & Casey 2009; Lo Faro et al. 2009; Magdis et al. 2010c; Pentericci et al. 2010; Oteo et al. 2013b; Bian et al. 2013; Bouwens et al. 2015; Oesch et al. 2015; Roberts-Borsani et al. 2016; Stefanon et al. 2017; Oesch et al. 2018).

The rest-frame ultraviolet (UV) light, mostly emitted by young and massive stars, has been commonly used as a star formation rate (SFR) tracer. However, the interstellar dust scatters or absorbs the UV light, and hence only a fraction of the energy output from star formation is observed in the UV. The rest is re-emitted in the infrared (IR) by the heated dust. The general pic-

ture of star formation activity across cosmic time peaks around $z \sim 2 - 4$ and significantly drops at $z > 4$ (see Madau & Dickinson 2014 for a review). The obscured star formation dominates the total SFR density (SFRD) over the redshift range $0 < z < 3$, and corresponds to half of the SFRD at $z = 3.6$ (Burgarella et al. 2013). Then, it is necessary to combine the UV and IR emission to determine the complete energy budget of star formation. However, because of the limited sensitivity of far-infrared (FIR) and radio observations, most of the current information at redshifts $z > 3 - 4$ are obtained from UV observations of LBG samples that need to be corrected for dust attenuation (e.g. Madau & Dickinson 2014).

Only a few LBGs have been directly detected at $z \sim 3$ in the mid-infrared (MIR) and FIR (Magdis et al. 2012; Casey et al. 2012; Oteo et al. 2013a) thanks to *Spitzer* and *Herschel*. This sample is biased against submillimeter bright galaxies and is not representative of the LBG population in terms of stellar mass (M_*), dust attenuation, and SFR (Burgarella et al. 2011; Oteo et al. 2013a). The recently gain in sensitivity with the Atacama Large Millimeter Array (ALMA) at submillimeter and millimeter wavelengths provides some insight into the obscured SFR at high- z (Capak et al. 2015; Bouwens et al. 2016; Fudamoto et al. 2017a; McLure et al. 2018). Even so, it is still very difficult to obtain large samples to carry out statistical and representative

analyses. Therefore, stacking analysis techniques (Dole et al. 2006) have been applied to relatively large samples of LBGs to derive their FIR/submillimeter emission (Magdis et al. 2010b,a; Rigopoulou et al. 2010; Coppin et al. 2015; Álvarez-Márquez et al. 2016; Koprowski et al. 2018).

Owing to the lack of FIR/submillimeter information of individual LBGs, empirical recipes are used to correct the UV emission for dust attenuation. The most commonly adopted is the relation between the UV continuum slope (β_{UV} , Calzetti et al. 1994) and the so-called IR excess ($IRX \equiv L_{IR}/L_{FUV}$) calibrated on local starburst galaxies by Meurer et al. (M99 hereafter; 1999). Despite its general use to infer the dust attenuation at high- z , there are several complications that make this method uncertain. The β_{UV} is known to be sensitive to the intrinsic UV spectra of galaxies, which depends on the metallicity (Z), age of the stellar population, and star formation history (SFH), and the shape of the dust attenuation curve. Stacking analyses of LBG and star-forming galaxies at redshifts of $1.5 < z < 5$ have shown different behaviors; some of these results follow the M99 relation (Magdis et al. 2010a; Reddy et al. 2012; Koprowski et al. 2018; McLure et al. 2018) and others lie above (Coppin et al. 2015; Bourne et al. 2017) or below this relation (Álvarez-Márquez et al. 2016; Bouwens et al. 2016; Reddy et al. 2018). These deviations have been shown to be driven by the stellar masses (Álvarez-Márquez et al. 2016; Bourne et al. 2017), the shape of the dust attenuation curve (Salmon et al. 2016; Lo Faro et al. 2017), and the sample selection (Buat et al. 2015). Direct detections of individual LBGs and IR-selected sources have suggested a large scatter in the IRX - β_{UV} plane (e.g., Oteo et al. 2013a; Casey et al. 2014; Fudamoto et al. 2017b). In addition, the stellar mass has been found to correlate with the dust attenuation, and its relation does not seem to evolve with redshift (Reddy et al. 2010; Buat et al. 2012; Heinis et al. 2014; Whitaker et al. 2014; Pannella et al. 2015; Álvarez-Márquez et al. 2016; Bouwens et al. 2016; Whitaker et al. 2017) at least in the intermediate range $1.0 < z < 4.0$.

With the objective to investigate deeply the dust attenuation in LBGs at high- z , a sample of 22,000 LBGs in the redshift range $2.5 < z < 3.5$ were selected in the COSMOS field (Scoville et al. 2007) and presented in a first publication (Álvarez-Márquez et al. 2016, AM16 hereafter). A statistically controlled stacking analysis from the FIR to millimeter wavelengths (100 μm to 1.1mm) was applied to derive their full IR spectral energy distribution (SEDs). Thanks to the large LBG sample, the stacking analysis was performed in different subsamples as a function of several parameters: L_{FUV} , β_{UV} , and M_* . We investigated the dust properties for each subsample of LBGs and studied their evolution in the IRX - β_{UV} , IRX - M_* , and IRX - L_{FUV} planes.

In this paper, we extend the initial work by applying a new stacking analysis from optical to millimeter wavelengths. This approach allows us to obtain the full rest-frame far-ultraviolet (FUV) to FIR SEDs of LBGs at $z \sim 3$, and derive the main physical parameters by mean of SED-fitting analysis techniques. This allows us to study the amount of dust attenuation and the shape of the dust attenuation curve that best represents the LBG population at $z \sim 3$. The outline of this paper is as follows. In Section 2, we describe the COSMOS field data and photometry used in our analysis. In Section 3, the definition of the LBG sample and its associated photometric redshift, M_* , L_{FUV} , and β_{UV} are presented. In Section 4, we define the method to stack the LBG sample from optical to FIR observations and obtain the stacked rest-frame FUV-to-FIR LBGs SEDs at $z \sim 3$. In Section 5, a SED-fitting analysis with CIGALE SED-fitting anal-

ysis code is performed on the stacked LBGs SED at $z \sim 3$ to derive their physical properties and build a library of semiempirical templates of LBGs at $z \sim 3$. In Section 6, we discuss the dust attenuation results obtained for the LBG sample in terms of the IRX and which dust attenuation curve is more likely to be representative for LBGs at $z \sim 3$. Finally, Section 7 presents the summary and conclusions.

Throughout this paper we use a standard cosmology with $\Omega_m = 0.3$, $\Omega_\Lambda = 0.7$, and Hubble constant $H_0 = 70 \text{ km s}^{-1} \text{ Mpc}^{-1}$, and the AB magnitude system. When comparing our data to others studies, we assume no conversion is needed for stellar mass estimates between Kroupa (2001) and Chabrier (2003) IMFs. To convert from Salpeter (1955) to Chabrier (2003) IMFs, we divide M_* Salpeter by 1.74 (Ilbert et al. 2010).

2. Data

We used the available optical to FIR imaging from the COSMOS field, and the optical/NIR multicolor catalog (Capak et al. 2007, version 2.0). The specific data sets are presented in the following Section.

2.1. Optical and near-infrared data

We used optical broadband imaging (B_J , V_J , r^+ , i^+ , z^{++}) from the COSMOS-20 survey (Capak et al. 2007; Taniguchi et al. 2007, 2015), observed at the prime-focus camera (Suprime-Cam) on the 8.2 m Subaru Telescope. In combination with the YJHK_s broadband imaging released in the UltraVISTA DR2¹ (McCracken et al. 2012) and observed with the VISTA *InfraRed CAMera* (VIRCAM) instrument on the *Visible and Infrared Survey Telescope for Astronomy* (VISTA). The original images have been homogenized to the same point spread function (PSF) with a full width at half maximum (FWHM) equal to 0.8'' by Laigle et al. (2016, private communication).

We additionally used optical/NIR broadband photometry (Subaru: B_J , V_J , g^+ , r^+ , i^+ , z^+ , and VISTA: Y , J , H and K_s) from the COSMOS multicolor catalog (Capak et al. 2007, version 2.0). The photometry was performed using SExtractor in dual-image mode over an aperture of 3'' centered at the position of the i^+ band detection. The COSMOS multicolor catalog was updated by Laigle et al. (2016), in which they provide a new NIR selection catalog on the ultra VISTA-DR2 observations. However, we still used the i -band selection catalog (Capak et al. 2007, version 2.0) because the LBG sample, used in this analysis (see Sect. 3), has been proposed to be detected at V_J and i^+ bands (AM16).

2.2. Mid- and far-infrared imaging

We use the *Infrared Array Camera* (IRAC: 3.6, 4.5, 5.8, and 8.0 μm) and the *Multiband Imaging Photometer for SIRTf* (MIPS: 24 μm) observations from the SCOSMOS survey (Sanders et al. 2007) as part of the *Spitzer* Cycle 2 and 3 Legacy Programs. The IRAC and MIPS observations present a 5σ flux sensitivity of 0.9, 1.7, 11.3, 14.9, and 80 μJy , respectively.

Herschel Space Observatory (Pilbratt et al. 2010) mapped the COSMOS field at 100 and 160 with the *Photodetector Array Camera and Spectrometer* (PACS; Poglitsch et al. 2010), and 250, 350, and 500 μm with the *Photometric Imaging Receiver* (SPIRE; Griffin et al. 2010) as part of the *Evolutionary Probe survey* (PEP; Lutz et al. 2011) and *Herschel Multi-*

¹ www.eso.org/sci/observing/phase3/data_release/uvista_dr2.pdf

Tiered Extragalactic Survey (HerMES, Oliver et al. 2012). The PACS images (100 and 160 μm) present point-source sensitivities of 1.5 mJy and 3.3 mJy and a PSF FWHM of 6.8'' and 11''. The SPIRE maps (250, 350, and 500 μm) have PSF FWHM of 18.2'', 24.9'', and 36.3'', 1σ instrumental noise of 1.6, 1.3, and 1.9 mJy beam⁻¹, and 1σ confusion noise of 5.8, 6.3, and 6.8 mJy beam⁻¹ (Nguyen et al. 2010). These maps were downloaded from HeDaM²

3. LBG sample

The LBG sample for this analysis is a subsample of that selected and characterized by AM16. The original LBG sample was selected in the COSMOS field by means of the classical U-dropout technique (Steidel et al. 1996) using the broadband filters u^* , V_J , and i^+ . This original sample contains ~ 22000 LBGs in the redshift range $2.5 < z < 3.5$ and UV luminosities $\log(L_{\text{FUV}}[L_\odot]) > 10.2$.

One of the objectives in this analysis is to perform a consistent rest-frame FUV to FIR stacking analysis. However, the available UltraVISTA survey ($YJHK_s$ bands) covers a reduced area of the COSMOS field of 1.5 deg². To be fully consistent and stack the same LBGs at any wavelength, we restricted the original LBGs sample to the limited area given by the UltraVISTA survey. Therefore, our final LBGs sample contains ~ 17000 LBGs, which are all LBG from the original sample enclosed in the UltraVISTA area.

3.1. Photometric redshift and stellar mass

We used the photometric redshifts (photo- z) and stellar masses computed by Ilbert et al. (2009, version 2.0) for i -band detected sources in the COSMOS field. The photo- z in the range $1.5 < z < 4$ were tested against the zCOSMOS faint sample and faint DEIMOS spectra, showing an accuracy of $\sim 3\%$ (Ilbert et al. 2009, version 2.0). The stellar masses were derived by applying SED-fitting techniques to the available optical and NIR photometry, and assuming; Bruzual & Charlot (2003) single stellar population (SSP), exponentially declining SFH, and Chabrier (2003) initial mass function (IMF). Ilbert et al. (2010) suggested that the i -band photometric redshift catalog is 90% complete at 5 μJy and 50% complete at 1 μJy in the IRAC 3.6 μm images.

3.2. Definition of L_{FUV} and β_{UV} for each LBG

The UV continuum slope, β_{UV} , is defined following the method presented by Finkelstein et al. (2012). They performed a rest-frame UV to optical SED-fitting analysis and obtained the β_{UV} by fitting a power law to the derived best-fit synthetic spectral model. In our case, we limited our LBG SEDs to the available optical-to-NIR broadband photometry (optical: B_J , V_J , g^+ , r^+ , i^+ , z^+ and NIR: Y , J , H and K_s) that lie at the rest-frame wavelength range $1000 < \lambda_{\text{rest-frame}} [\text{\AA}] < 3500$. This allows us to perform an SED-fitting analysis over the same rest-frame spectral range for each LBGs independent of its redshift.

We used CIGALE (Code Investigating GALaxy Emission; Burgarella et al. 2005; Noll et al. 2009; Boquien et al. 2019, see Sect. 5) to perform the rest-frame UV-to-optical SED-fitting analysis and derive the best-fit model spectrum for each LBG of the sample. We assume Bruzual & Charlot (2003) synthetic stellar population libraries and Chabrier (2003) IMF. We varied

the metallicity ($0.02 < Z [Z_\odot] < 1.00$), age of the stellar population ($1 \text{ Myr} < t < t_H$), dust extinction ($0 < A_V < 2 \text{ mag}$, using the Calzetti et al. (2000) dust attenuation law), and SFH (SFH $\propto e^{-t/\tau}$, where $\tau = 0.1, 10, 100, 10^3, 10^4, 10^5, -300, -10^3, -10^4$ Myr).

The value β_{UV} is calculated by power-law fit ($f_\lambda \propto \lambda^{\beta_{\text{UV}}}$) to the best-fit synthetic stellar population model that has been derived by CIGALE. The power-law fit is performed at rest-frame wavelength range $1250 < \lambda_{\text{rest-frame}} [\text{\AA}] < 2000$ following the spectral windows defined by Calzetti et al. (1994). We excluded the range $2000 < \lambda [\text{\AA}] < 2600$ for two reasons: i) to omit the dust feature at 2175 \AA and ii) to have a homogeneous rest-frame wavelength range independent of the redshift of the galaxy. The value L_{FUV} is computed in a squared bandpass defined as the GALEX FUV band ($\lambda_{\text{eff}} = 152.8 \text{ nm}$ and effective bandwidth = 11.4 nm). We checked the uncertainties in the β_{UV} and L_{FUV} estimations using the mock analysis tool from CIGALE (see Sect. 5.2 for details of the mock analysis tool). We obtained a dispersion in the β_{UV} of $\Delta\beta_{\text{UV}} \sim 0.2$ and a very robust L_{FUV} measure with $\Delta \log(L_{\text{FUV}}[L_\odot]) \sim 0.03$. Additionally, we obtained a systematic offset between the β_{UV} calculated by power-law fit directly to the photometry (AM16) and that derived from power-law fit to the best-fit model obtained by SED-fitting analysis of the photometry (see Appendix A for a detailed discussion).

4. Stacking analysis

Stacking analysis is a technique to determine the mean flux density of a population of sources that are individually too dim to be detected in a confusion-limited maps (e.g., Dole et al. 2006; Marsden et al. 2009; Béthermin et al. 2012; Heinis et al. 2013). Our LBG sample is complete at V_J and i^+ bands, where the sample has been selected by means of the U-dropout technique. However, the detection of individual LBGs at other optical/NIR bands are dropped up to 70% of completeness, and it gets worse at longer wavelengths as far as only few of the LBGs could be detected at FIR observations (SPIRE 250 μm). We then decided to average the signals of multiple LBGs from optical-to-FIR observations to obtain fully consistent mean rest-frame FUV-to-FIR SEDs of LBGs at $z \sim 3$. This allows us to detect statistically the LBG population at redder wavelength at the expense of averaging over their individuals properties.

Previous works that computed average rest-frame FUV-to-FIR LBG SEDs (e.g., Magdis et al. 2010a) performed a simple average to the optical/NIR photometry. Our LBG sample is 70-80% complete at NIR and 90-100% complete at optical bands. Then, we decided to perform a stacking analysis in the optical/NIR to eliminate a possible bias to the brightest LBGs (if only detected LBGs are averaged).

We split our LBG sample as a function of L_{FUV} , β_{UV} , and M_* in five different ways. The first three are done as a function of the single parameters L_{FUV} , β_{UV} , and M_* . For the two others, we split the sample as a function of the combination of β_{UV} and M_* in the (β_{UV}, M_*) plane. Table 1 shows the sample binning. It includes the interval used to define each bin, the number of LBGs that are stacked, and the mean values of L_{FUV} , β_{UV} , M_* , and redshift that define each bin. The uncertainties associated with the average values are defined by the standard deviation of the mean. The number of bins and the intervals are optimized to obtain a good signal-to-noise ratio (S/N) on the final FIR (SPIRE bands) stacked images.

² Herschel Database in Marseille: <http://hedam.lam.fr/HerMES/>

Table 1: Sample binning

ID	Range	$\log(L_{\text{FUV}}[L_{\odot}])$	$\log(M_{*}[M_{\odot}])$	β_{UV}	z	N_{gal}
Stacking as a function of L_{FUV} (LBG-L)						
LBG-L1	10.2 - 10.5	10.35±0.09	9.67±0.47	-1.51±0.45	3.00±0.23	9145
LBG-L2	10.5 - 10.8	10.63±0.09	9.78±0.44	-1.56±0.41	3.08±0.25	5385
LBG-L3	10.8 - 11.1	10.91±0.08	9.94±0.37	-1.54±0.36	3.11±0.25	1510
LBG-L4	11.1 - 11.4	11.20±0.08	10.14±0.38	-1.54±0.32	3.15±0.24	199
Stacking as a function of β_{UV} (LBG- β)						
LBG- β 1	-1.7 - -1.1	10.49±0.24	9.75±0.44	-1.42±0.17	2.99±0.25	8531
LBG- β 2	-1.1 - -0.7	10.41±0.22	9.88±0.62	-0.94±0.11	2.94±0.24	2445
LBG- β 3	-0.7 - -0.3	10.30±0.20	10.00±0.66	-0.54±0.10	2.91±0.21	593
LBG- β 4	-0.3 - 0.3	10.26±0.21	10.17±0.72	-0.10±0.21	2.89±0.21	114
Stacking as a function of stellar mass (LBG-M)						
LBG-M1	9.75-10.00	10.51±0.24	9.86±0.08	-1.45±0.38	3.05±0.25	4517
LBG-M2	10.00-10.25	10.55±0.26	10.10±0.08	-1.29±0.41	3.02±0.26	2257
LBG-M3	10.25-10.50	10.58±0.29	10.35±0.08	-1.14±0.43	2.98±0.26	1041
LBG-M4	10.50-10.75	10.55±0.27	10.60±0.08	-1.08±0.45	2.95±0.26	372
LBG-M5	10.75-11.00	10.52±0.31	10.86±0.08	-0.95±0.43	2.94±0.25	160
LBG-M6	11.00-11.50	10.47±0.28	11.16±0.12	-0.77±0.51	2.96±0.24	55
Stacking as a function of (β_{UV}, M_{*}) - LBG-M β 1						
LBG-M β 1- $M_0\beta_0$	(-1.7 - -1, 9.75-10.65)	10.55±0.25	10.00±0.20	-1.35±0.20	3.02±0.25	4799
LBG-M β 1- $M_0\beta_1$	(-1 - -0.5, 9.75-10.65)	10.41±0.22	10.12±0.23	-0.82±0.14	2.93±0.24	1343
LBG-M β 1- $M_0\beta_2$	(-0.5 - 0.3, 9.75-10.65)	10.26±0.19	10.18±0.23	-0.32±0.16	2.87±0.21	208
LBG-M β 1- $M_1\beta_0$	(-1.7 - -1, 10.65-11.50)	10.62±0.31	10.83±0.16	-1.28±0.19	2.97±0.26	146
LBG-M β 1- $M_1\beta_1$	(-1 - -0.5, 10.65-11.50)	10.44±0.20	10.84±0.16	-0.78±0.14	2.89±0.23	122
LBG-M β 1- $M_1\beta_2$	(-0.5 - 0.3, 10.65-11.50)	10.35±0.20	10.95±0.20	-0.41±0.05	2.90±0.22	40
Stacking as a function of (β_{UV}, M_{*}) - LBG-M β 2						
LBG-M β 2- $M_0\beta_0$	(-1.7 - -0.8, 9.75-10.125)	10.51±0.23	9.91±0.11	-1.31±0.23	3.01±0.25	4056
LBG-M β 2- $M_0\beta_1$	(-0.8 - 0.3, 9.75-10.125)	10.27±0.16	9.95±0.11	-0.60±0.19	2.94±0.22	338
LBG-M β 2- $M_1\beta_0$	(-1.7 - -0.8, 10.125-10.5)	10.61±0.28	10.27±0.10	-1.22±0.23	2.99±0.26	1373
LBG-M β 2- $M_1\beta_1$	(-0.8 - 0.3, 10.125-10.5)	10.37±0.21	10.29±0.10	-0.56±0.21	2.88±0.21	337
LBG-M β 2- $M_2\beta_0$	(-1.7 - -0.8, 10.5-10.75)	10.59±0.27	10.61±0.07	-1.19±0.25	2.96±0.26	260
LBG-M β 2- $M_2\beta_1$	(-0.8 - 0.3, 10.5-10.75)	10.40±0.22	10.60±0.08	-0.52±0.23	2.87±0.25	86
LBG-M β 2- $M_3\beta_0$	(-1.7 - -0.8, 10.75-11)	10.59±0.31	10.85±0.07	-1.18±0.23	2.94±0.25	102
LBG-M β 2- $M_3\beta_1$	(-0.8 - 0.3, 10.75-11)	10.35±0.18	10.86±0.08	-0.49±0.27	2.91±0.23	53
LBG-M β 2- $M_4\beta_0$	(-1.7 - -0.8, 11-11.5)	10.58±0.29	11.14±0.13	-1.15±0.24	3.04±0.26	27
LBG-M β 2- $M_4\beta_1$	(-0.8 - 0.3, 11-11.5)	10.40±0.24	11.18±0.12	-0.38±0.26	2.88±0.18	26

4.1. General method

The general method used to perform the optical-to-FIR stacking analysis is based on the IAS library (Bavouzet 2008 and Béthermin et al. 2010)³. Given a specific catalog and field image, the library extracts square cutout images centered on each source and stores these images in a cube. Then, it generates a stacked image by averaging them. Additionally, it rotates each image by $+\pi/2$ with respect to the previous image to cancel out the large-scale background gradients. To get valid and reliable results, the general method has to be corrected for different effects that generate a nonhomogeneous background on the stacked image (Bavouzet 2008; Béthermin et al. 2010; Heinis et al. 2013; AM16). The following three points are of major importance:

1. Correction for clustering of the input catalog. The LBGs are clustered between them and other star-forming galaxies at high redshift. Depending on the PSF size of the available observations, the PSF beam may be contaminated by different nearby sources included in the same sample. Therefore, we could account for the flux of the same source more than once during the stacking analysis. This effect would lead to an overestimation of the mean flux due to the clustered nature of the sources. It is corrected by taking into account the angular correlation function of the input catalog. The complete formalism is detailed in AM16.
2. Correction for incompleteness of the input catalog in the dense regions. A bias is produced in the stacked image when the population of sources is not complete (Dole et al. 2006;

Bavouzet 2008; Béthermin et al. 2010; Heinis et al. 2013; Viero et al. 2013). If the stacked sample presents a relatively high percentage of incompleteness, part of the faint LBG population (mostly located in the crowded areas of the image or close to bright objects) are missed during the source extraction process at optical images. When we move to longer wavelength observation (e.g., FIR), the optical crowded areas and the bright objects contribute to enlarge the local background level. This means that if we perform the stacking analysis on an incomplete population, we would mostly stack the areas in which the background presents lower levels and lose the contribution of the areas with higher levels. It produces a negative contribution in the central part of the stacked image related to the global background level. We corrected this effect using extensive simulations to characterize the detection process and sample selection. We performed these simulations by injecting mock sources in the original images (V_j and i^+ bands), and keeping track of the recovered sources. The full formalism used to correct this effect is deeply explained in AM16.

3. Correction for bright field sources in crowded field observations. A deep observation, not dominated by the confusion noise, generates a crowded field image. The presence of a large number of bright neighbors may generate an additional noise level that perturbs the final stacked image. We removed the contribution of field sources in our stacking procedure by performing a weighted stacking analysis to mask them. We proceeded as follows:

- We generated a segmentation map, using SExtractor (Bertin & Arnouts 1996), on the image where the stack-

³ <http://www.ias.u-psud.fr/irgalaxies/downloads.php>

ing analysis is performed. A source extraction was applied to detect all the objects with flux larger than $3\sigma_{Back}$, excluding the LBGs from our sample.

- We created a weight map by assigning a value equal to 1 for background pixels and equal to 0 for detected source pixels.
- We performed the stacking analysis by using a weighted mean, $\sum_i I_i W_i / \sum_i W_i$, for each individual pixel of the cutout image. Where i corresponds to each object inside the sample, I_i one of the pixels from the cutout image extracted from the map, and W_i one of the pixels from the cutout image extracted from the weighted map.

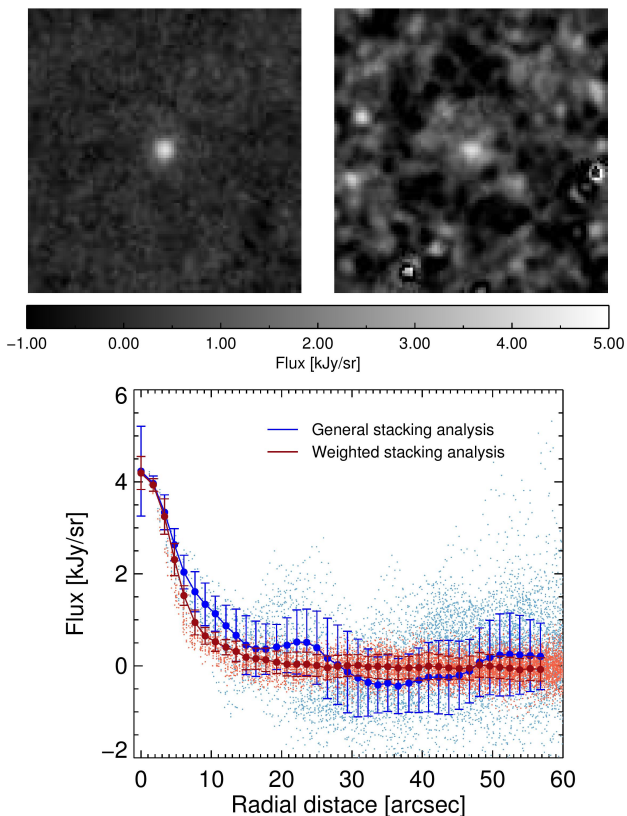


Fig. 1: Top panel: Maps of the final MIPS stacked images for the first bin as a function of the L_{FUV} ($10.2 < \log(L_{FUV}[L_{\odot}]) < 10.5$). The left panel shows the stacked image using the weighted stacking analysis and the right image using the general stacking method. The bottom panel shows the radial profiles estimated from the upper images. The blue line corresponds to the stacking analysis performed using the general method, and the red line correspond to the stacking analysis performed using the weighted method. The lighter blue and red points correspond to the value of each pixel from the stacked images.

Figure 1 shows the improvement that we get in the final stacked image using a weighted stacking analysis for the $24 \mu\text{m}$ MIPS observations. This example corresponds to the final stacked image, with and without applying the weighted procedure, for one of the bins of the stacking analysis as a function of L_{FUV} . This new method provides a considerable improvement in the background noise, which is essential to detect and recover the emission of the stacked population.

Each of these corrections impacts at various levels the final stacked image, which mainly depends on the image quality (PSF, confusion noise, and depth), observed wavelength, and sample selection method. In Sections 4.2, 4.3, and 4.4, we discuss which of the previous corrections are taken into account during the stacking analysis for each of the data sets.

4.2. Far-infrared analysis

The following procedure is applied to perform the stacking analysis on PACS (100 and $160 \mu\text{m}$) and SPIRE (250, 350, and $500 \mu\text{m}$) images. It was previously used and explained well in AM16. We used the calibrated PACS and SPIRE maps without cleaning the images from any detected source, and we did not apply the correction for bright field sources in crowded field observations to mask the bright neighbors during the stacking procedure. If a large number of sources were stacked in confusion limit maps, as in our FIR images, the bright neighbors tend to average homogeneously to a constant background level. We demonstrated this by performing a random stacking analysis at the same number of positions than objects in each of our sample bins.

The PACS and SPIRE observations present large PSF sizes, with FWHM PSFs that vary from $6''$ to $36.3''$. Our LBG sample is clustered and could be defined by an autocorrelation function, $\omega[\theta, \phi] \propto \theta^{-\gamma}$, with $\gamma = 0.63$ (AM16). The combination of large PSF sizes and the clustered nature of our LBG sample could produce a contamination of our LBG PSF beams due to a nearby LBGs. If we stack them, we account for the flux of the same source more than once during the stacking analysis. Therefore, we applied the correction for clustering of the input catalog to deconvolve the emission of our LBG population and the clustering contribution. Additionally, we corrected our stacking analysis for the incompleteness of the input catalog in the dense regions following the analysis done in AM16.

4.3. Mid-Infrared analysis

The following procedure is applied to perform the stacking analysis for IRAC (3.6, 4.5, 5.8, $8 \mu\text{m}$) and MIPS ($24 \mu\text{m}$) observations. The IRAC images present a PSF FWHM equal to $1.66''$, $1.72''$, $1.88''$, and $1.98''$ with a pixel size of $0.6''$, and the MIPS observation has a PSF FWHM equal to $6''$ and a pixel size of $1.2''$. The improvement of the PSF FWHM size and sensitivity from FIR to MIR observations reduces the confusion noise and improves the quality of the MIR images. This generates a crowded image with a large number of field sources. The presence of the large amount of field sources in the maps generates an additional noise level and clustering contribution that perturbs our stacked images. To remove this effect from our stacked sources, we applied the weighted stacking analysis previously presented in the correction for bright field sources in crowded field observations.

The reduction of the PSF FWHM sizes from FIR to MIR maps lowers and makes negligible the clustering effect on the stacked LBGs. Therefore, here, we did not take into account any corrections related to the clustering nature from our input LBGs population in the stacked LBGs. However, the bias induced in our stacked image due to the incompleteness of our input catalog is still present. We realized that this effect decreases when the stacking procedure is performed closer to the sample selection wavelengths (V_j and i^+ bands). However, it is still important to correct for this effect in the MIR wavelength.

We performed an aperture photometry to calculate the flux density of the stacked LBGs in the IRAC and MIPS observations. We made a circular aperture with radius equal to 3.6'' and 7'', and a background annulus from 3.6'' to 8.4'' and 20'' to 32''. We then applied an aperture correction of 1.125, 1.120, 1.135, 1.221, and 1.61 at IRAC (3.6, 4.5, 5.8, 8 μm) and MIPS (24 μm)⁴. We used bootstrap resampling to obtain the mean values and errors. We repeated the above procedure over 3000 random bootstrap samples and adopted 1 σ of the distribution of the derived fluxes as the uncertainty for our results. Appendix C presents the derived fluxes and uncertainties of our stacking analysis at FIR and MIR. This appendix includes the stacking analysis performed for AzTEC (1.1mm), and previously presented in AM16.

4.4. Optical/near-infrared analysis

The following procedure is applied to perform the stacking analysis in the optical (B_J , V_J , r^+ , i^+ , z^{++} bands) and NIR (Y , J , H , K_s) observations. The optical and NIR images have a homogenized PSF with a FWHM equal to 0.8'', and a large depth improvement with respect to the MIR observations. The optical/NIR observations contain large number of bright field sources that are removed by performing a weighted stacking analysis. We did not apply any corrections related to the clustering nature of our sample and the incompleteness of our input catalog. These two effects are negligible in our stacked optical/NIR images.

We computed the photometry on the stacked object by fitting a Moffat function. The error is calculated by combining the contribution of different effects: bootstrap, error in the fitting procedure, and Poisson noise. Appendix B presents the derived fluxes and uncertainties of our stacking analysis in optical and NIR wavelengths. We verified the method by comparing the derived stacked fluxes with an average observed photometry of individual LBGs at V_J and i^+ bands, where the sample is complete. In both cases, we obtain results within the derived uncertainties.

5. SED-fitting analysis

A Python-based modular code, CIGALE (Burgarella et al. 2005; Noll et al. 2009; Boquien et al. 2019)⁵ is dedicated to fitting SEDs from the UV to the FIR and to creating galaxy emission models in the same wavelength range. The CIGALE code is modular and allows the user to create models by selecting independent modules for parameters such as the SFH, stellar models, shape of the dust attenuation curve, nebular emission, contribution of an active galactic nuclei, and dust emission templates or models.

5.1. Initial parameters

Deriving physical properties of galaxies by fitting synthetic SEDs to a multiband photometry requires making prior assumptions on the initial parameters to build the synthetic SED library. Assumptions such as SFH, IMF, metallicity, and dust attenua-

⁴ The photometry configuration and aperture correction have been obtained from the instrument handbook of IRAC (<http://irsa.ipac.caltech.edu/data/SPITZER/docs/irac/iracinstrumenthandbook/27/>), and MIPS (<http://irsa.ipac.caltech.edu/data/SPITZER/docs/mips/mipsinstrumenthandbook/50/>)

⁵ Code Investigating GALaxy Emission (CIGALE): <https://cigale.lam.fr/>

tion curve affect the derived galaxy properties like the SFR, stellar mass, age of the stellar population, amount of dust attenuation (e.g., Papovich et al. 2001; Maraston et al. 2010; Pforr et al. 2012; Schaerer et al. 2013; Buat et al. 2014; Lo Faro et al. 2017). Table 2 summarizes the initial parameters used to perform the SED-fitting analysis for our stacked LBGs SEDs at $z \sim 3$.

Table 2: Initial parameters used in the SED-fitting analysis

Parameter	Symbol	Range
SFH (Delay- τ)		
age	age	10 to 2000 Myr
e-folding timescales	τ	20 to 1500 Myr
SSP (Bruzual & Charlot 2003)		
Initial mass function	IMF	Chabrier (2001)
Metallicity	Z	Fixed to 0.2Z $_{\odot}$
Dust attenuation (Noll et al. 2009)		
Color excess	E(B-V)	0.025 to 1.5
Slope of the power law	δ	-0.5 to 0.5
UV bump at 2175Å		Not included
Dust emission (Draine & Li 2007)		
Mass fraction of PAH	p_{PAH}	fixed to 3.9%
Minimum radiation field	U_{min}	0.7 to 50
Power slope $dU/dM \propto U^{-\alpha}$	α	fixed to 2.0
Dust fraction in PDRs	γ	0.01 to 0.04

We adopted the stellar population models from Bruzual & Charlot (2003) and an IMF from Chabrier (2001). Delayed SFHs ($SFR \propto t/\tau^2 e^{-t/\tau}$), with varying e-folding times are assumed to model the SFH of our LBGs at $z \sim 3$ (Lee et al. 2010). We performed a test to check the influence of the chosen SFH on the final derived physical parameters, where we ran CIGALE with different SFHs recipes (exponential declining, exponential rising, constant, and delayed) using the same initial parameters from Table 2. The results suggest that our SED-fitting analysis cannot distinguish which of the tested SFHs recipes are more likely to reproduce the LBG population. Nevertheless, our SED-fitting analysis can derive fully consistent physical parameters independent of the SFH chosen with the exception of the age of the stellar population.

The metallicity was fixed to 0.2 Z $_{\odot}$ (Castellano et al. 2014). We fixed the metallicity because i) the SED-fitting technique applied to broadband photometry can hardly constrain the metallicity due to the age-dust-metallicity degeneracy (López Fernández et al. 2016), and ii) the metallicity of our stacked SEDs are averaged due to the combination of a large number of galaxies. However, there is a possibility to have an evolution of metallicity in our LBG sample due to the well-known mass-metallicity relation (e.g., Mannucci et al. 2009). Then, we performed an individual SED-fitting analysis for the stacking analysis as a function of M_* with the metallicity as a free parameter. The derived physical parameters are in agreement, within the uncertainties, with those from the fixed metallicity. Therefore, we concluded that our choice of fixed metallicity does not have a large impact on the final derived physical parameters.

Dust attenuation is treated using the prescription given by Noll et al. (2009) in Eq. 1. These authors used the Calzetti dust attenuation law ($k(\lambda)$, Calzetti et al. 2000) as a baseline. This provides the possibility to i) include a UV bump at 2175 Å modeled by a Lorentzian-like profile, and ii) modify the slope of the dust attenuation curve by a power law,

$$A(\lambda) = \frac{A_V}{4.05} \left(k(\lambda) + D_{\lambda_0, \gamma, E_{bump}} \right) \left(\frac{\lambda}{\lambda_V} \right)^{\delta}, \quad (1)$$

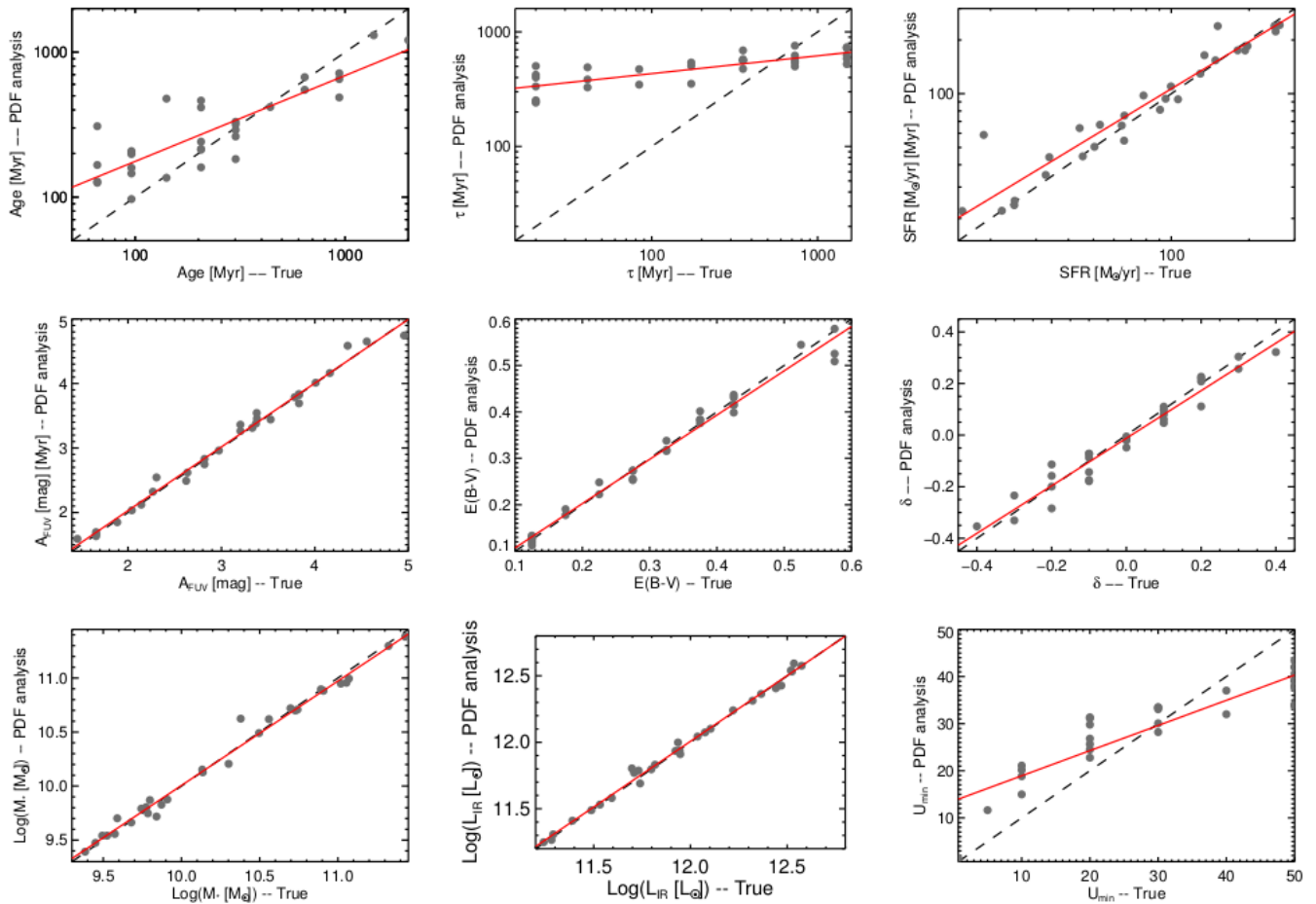


Fig. 2: CIGALE mock analysis results. On the x-axis the *true* parameter values are provided by the best-fit model + noise constitute the mock SED catalog. These true values are compared with the PDF value estimated by CIGALE on the y-axis. The 1-1 correlation line is shown as a black long dashed line in each panel. From top left to bottom right, we show the results for the age of the stellar population, e-folding timescale of delay- τ SFH, SFR, FUV dust attenuation, $E(B-V)$, slope of the dust attenuation curve - δ , stellar mass, total IR luminosity, and U_{min} . The regression lines for each assumed configuration are also plotted as red solid lines.

where $A(\lambda)$ is the modified dust attenuation curve presented by Noll et al. (2009), A_V is the dust attenuation in the V band, $D_{\lambda_0, \gamma, E_{bump}}$ is the UV bump profile, δ is the power-law slope with respect to the Calzetti's law, and $\lambda_V = 5500 \text{ \AA}$. The shape of the dust attenuation curve depends on the stardust geometry, grain size distribution, etc. (Witt & Gordon 2000a). Complex dust geometries can produce a grayer or shallower dust attenuation curve than Calzetti's law (Buat et al. 2011a; Kriek & Conroy 2013; Zeimann et al. 2015; Salmon et al. 2016; Lo Faro et al. 2017). Our SED fitting takes δ as a free parameter to mimic the variation on the shape of the dust attenuation curve. The absorption feature produced by dust at 2175 \AA , UV bump, is set to zero because the stacked SEDs do not have enough spectral resolution to constrain it.

The IR emission is modeled using Draine & Li (2007) dust models. The validity of these models to reproduce the FIR emission of Herschel detected high- z main sequence galaxies was confirmed by Magdis et al. (2012). The dust models require the fine-tuning of several free parameters: the mass fraction of PAH (polycyclic aromatic hydrocarbons, q_{PAH}), minimum and maximum radiation field (U_{min} , U_{max}), power slope $dU/dM \propto U^{-\alpha}$ (α), dust fraction in PDRs (γ), and dust mass (M_{dust}). However,

Draine & Li (2007) showed that fixed values of $\alpha = 2$ and $U_{max} = 10^6$ can reproduce the SEDs of galaxies with a wide range of properties. The stacked SEDs only have the information of MIPS $24 \mu\text{m}$ (rest-frame $6 \mu\text{m}$) in the PAH part of the spectrum, which is not enough to constrain the q_{PAH} . After some initial tests with the q_{PAH} as a free parameter, we fixed q_{PAH} to 3.9%. This value best fit our SEDs by eye even though it is higher than that proposed by Magdis et al. (2012), who found an interval from 1.12% to 3.19%. We consider U_{min} to vary between 0.7 to 50. Draine & Li (2007) suggested using $U_{min} > 0.7$ because lower values correspond to dust temperatures below $\sim 15\text{K}$, which we cannot constrain by our FIR photometry alone. The fraction of dust enclosed in the PDRs was fixed by Magdis et al. (2012) to $\gamma=0.02$, and Draine & Li (2007) suggested that the γ value should not be higher than 0.04 (4%). We detected some variations at rest-frame wavelength 20-50 μm for our set of stacked SEDs, which suggest different γ values. Therefore, we used a γ range from 0.01 to 0.04.

The adopted initial configuration (Table 2) gives a total of 609840 synthetic galaxy models/SEDs. This set of models is used to perform the SED fitting and Bayesian analysis over our 30 rest-frame FUV-to-FIR stacked LBGs SEDs at $z \sim 3$.

5.2. Physical parameters for LBGs at $z \sim 3$

We ran CIGALE for the sample of 30 rest-frame FUV-to-FIR stacked LBGs SEDs at $z \sim 3$. We used the adopted initial configuration listed in Table 2. The CIGALE code estimates and derives the physical parameters, such as stellar mass, dust mass, age of stellar populations, SFR, rest-frame IR and FUV luminosities, FUV attenuation, and β_{UV} , as well as the input parameters from Table 2. Additionally, CIGALE provides the synthetic model that best fits the observational SEDs by χ^2 minimization.

The CIGALE code uses a Bayesian analysis to derive the physical parameters. This code builds the probability distribution function (PDF) for each parameter, and takes its mean and standard deviation (Noll et al. 2009; Boquien et al. 2019). We used a mock analysis to check the robustness, accuracy, and parameter degeneracy of our estimates. The mock analysis consists in generating a mock catalog of artificial SEDs, similar to the input LBGs, for which the physical parameters have been previously derived, and adding a Gaussian noise where the dispersion is taken from the observed uncertainty. Then, we compared these values with the CIGALE estimates (more details: Buat et al. 2012; Ciesla et al. 2015; Lo Faro et al. 2017; Boquien et al. 2019). This procedure allows us to check our ability in estimating and constraining the individual output parameters given the information provided by the detailed shape of the broadband SED. The results are summarized in Figure 2. We call the parameter value provided by the best-fit model “true” and used this value to compute the mock SEDs. This “true” parameter value, on the x-axis, is compared with the PDF value, on the y-axis, which is computed by SED-fitting analysis over the mock SEDs catalog. From top left to bottom right, Figure 2 shows the results for the age of the stellar population, e-folding timescale of delay- τ SFH, SFR, FUV dust attenuation, E(B-V), change of the slope of the dust attenuation law with respect to Calzetti - δ , stellar mass, total IR luminosity, and U_{min} . On the one hand, the results emphasize that we are not able to determine the shape of the SFH and age of the stellar population by SED-fitting analysis. The estimated PDFs of the e-folding timescale, τ , appear to average out to a constant value independent of the true value used to compute the mock SEDs. The age of the stellar population is slightly constrained for the particular case of delay- τ SFH model, but it is biased against the chosen SFH. On the other hand, the results suggest that our procedure well constrain the physical parameters: stellar mass, IR luminosity, FUV dust attenuation, SFR, and change of the slope of the dust attenuation law with respect to Calzetti - δ , with the chosen delay- τ SFH. In Section 5.1, we also conclude that these physical parameters are not affected by the chosen SFH. Therefore, despite of the degeneracy for the SFH and ages of the stellar population, our SED-fitting analysis provides consistent physical parameters.

Appendix D lists the input and additional physical parameters derived by SED-fitting analysis in the 30 stacked LBGs SEDs. The β_{UV} and L_{UV} are computed in a separate FUV-optical SED-fitting analysis; the input parameters and procedure are already explained in Section 3.2.

5.3. Templates of LBGs at $z \sim 3$

We used the results from the panchromatic stacking and SED-fitting analysis to build a library of empirical rest-frame FUV-to-FIR templates of LBGs at $z \sim 3$.⁶ The library contains 30 empir-

⁶ Templates and SEDs are only available at the CDS via anonymous ftp to cdsarc.u-strasbg.fr (130.79.128.5) or via http://cdsarc.u-strasbg.fr/viz-bin/cat/J/A+A/630/A153

ical SEDs and their best-fit synthetic model spectrum. The empirical SEDs correspond to the rest-frame FUV-to-FIR stacked LBGs SEDs derived by stacking analysis in Section 4. These SEDs result from combining ~ 17000 individual LBGs in different bins as a function of L_{FUV} , M_* , β_{UV} , and a combination of M_* and β_{UV} . More specifically, the number of individual LBGs used to obtain each stacked LBG SED varies from about 9000 to 100. This statistics strengthens our library in the sense that our SEDs have an exceptional S/N, which is not comparable with any individual detected LBG at $z \sim 3$. The set of synthetic model spectrum associated with each stacked LBG SED is obtained with CIGALE.

Thanks to the binning configuration used to split our large LBG sample, we derived a set of templates with a large variety of physical properties. Our library contains templates within an interval of stellar mass, $9.2 < \log(M_* [M_\odot]) < 11.4$; SFR, $20 < SFR [M_\odot \text{yr}^{-1}] < 300$, β_{UV} , $-1.8 < \beta_{UV} < -0.2$; FUV dust attenuation, $1.5 < A_{FUV} [mag] < 4.8$; IR luminosity, $11.2 < \log(L_{IR} [L_\odot]) < 12.7$; and FUV luminosity, $10.4 < \log(L_{FUV} [L_\odot]) < 11.2$. This variety makes our library versatile in the sense that our templates fit a wide range of physical properties for star-forming galaxies at $z \sim 3$.

Figure 3 shows the four SEDs and templates derived in the stacking analysis as a function of L_{FUV} . If a sample binning is carried out as a function of L_{FUV} , the subsample becomes a mix of red, blue, high, and low-mass galaxies. For example, a massive red galaxy with a large dust attenuation may have the same L_{FUV} than a low-mass blue galaxy. Therefore, if a stacking analysis is applied to a mix population of LBGs, the final results tend to average to a similar mean SED with a different normalization factor, i.e., L_{FUV} . Figure 3 shows the rest-frame FUV-to-NIR part of the SEDs presents a similar behavior except for the lowest L_{FUV} bin, which has a slightly bluer β_{UV} . We can also see this from the derived physical properties on the SED-fitting analysis, where we only find differences in the bolometric luminosity, M_* and SFR, which is associated with an increase of the normalization factor. However, the FIR peak has progressively shifted to longer wavelengths for higher L_{FUV} , which suggests a lower mean dust temperature. If we consider that the U_{min} values are correlated with the location of the FIR peak (Draine & Li 2007; Magdis et al. 2012). This behavior is reinforced by the variation of the U_{min} values ($38.5 < U_{min} < 19.2$), derived from our SED-fitting analysis, for the lowest to the highest L_{FUV} bin.

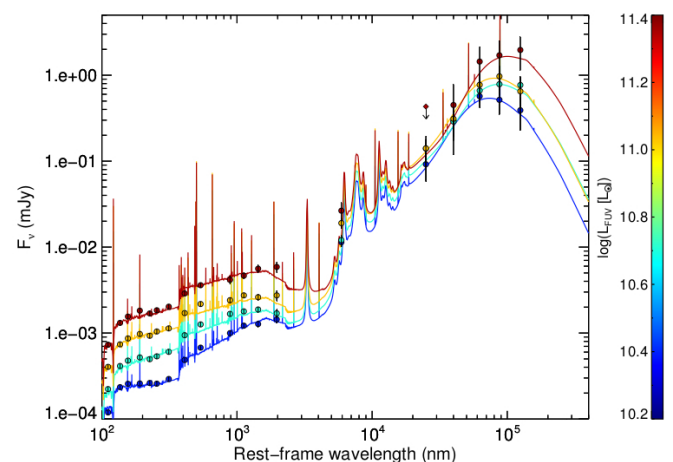


Fig. 3: Stacked LBGs SEDs and the best-fit models for the stacking as a function of L_{UV} .

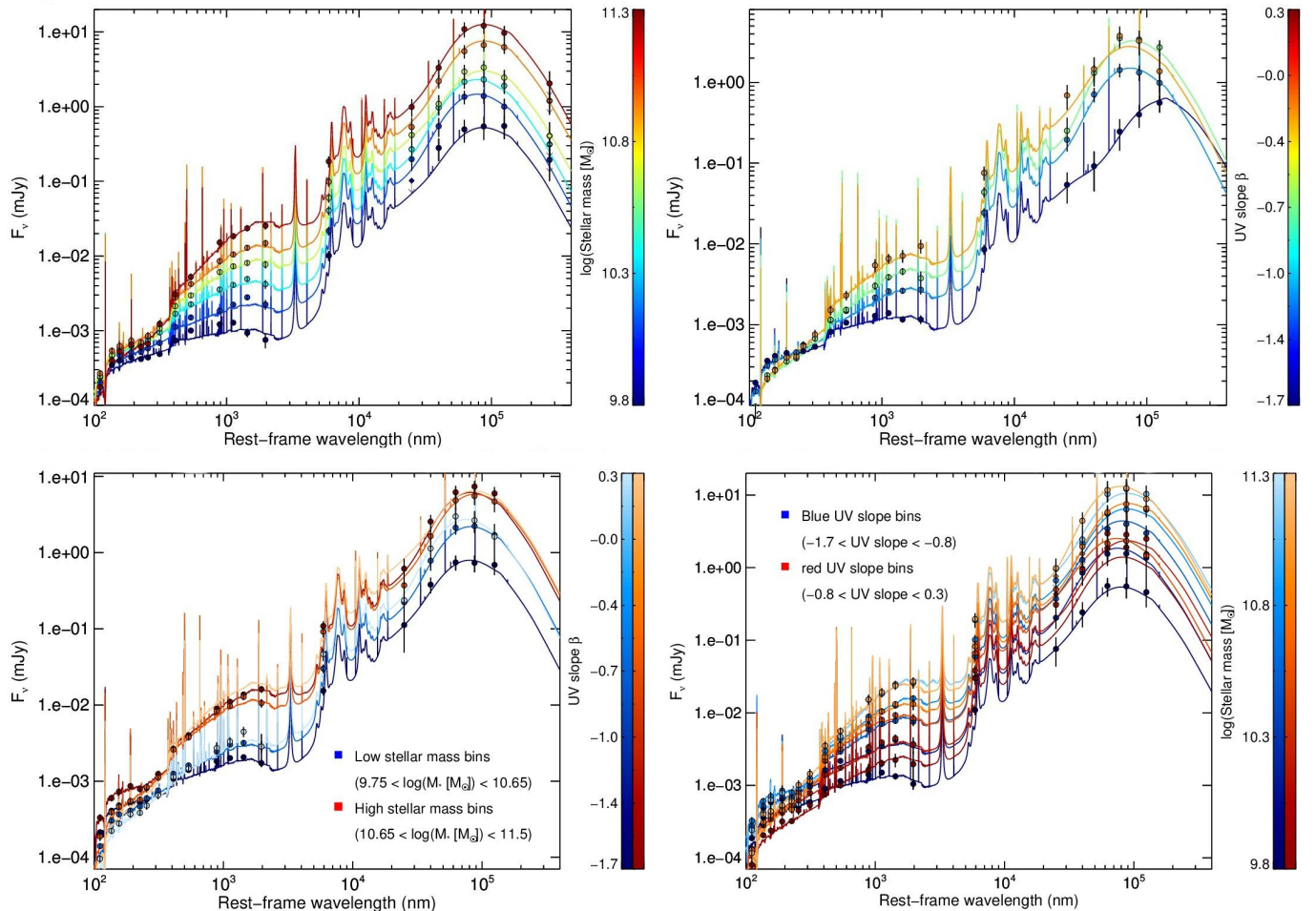


Fig. 4: Stacked LBGs SEDs and the best-fit models for the stacking analyses as a function of M_* (top left panel) and β_{UV} (top right panel). The bottom panel shows the LBG- $M\beta 1$ (left) and LBG- $M\beta 2$ (right) stacking analyses, which are derived from a combination of both, M_* and β_{UV} , in the M_* and β_{UV} plane.

The top left panel of Figure 4 illustrates the six SEDs and templates derived from the stacking analysis as a function of M_* . Their rest-frame FUV-to-NIR SEDs present an increase of the rest-frame NIR flux, which is well known to correlate with M_* (Kauffmann & Charlot 1998), and a reddening of the UV/optical part of the spectrum. No significant variations are found in the shape of the FIR emission, but the IR luminosity increases proportionally with M_* . The top right panel of Figure 4 shows the four SEDs and templates derived from the stacking analysis as a function of β_{UV} . Their rest-frame FUV-to-NIR SEDs have higher rest-frame NIR flux for redder β_{UV} , and the slope of the UV spectrum follows the mean β_{UV} of the stacked population. The FIR emissions present similar shapes with an increase of L_{IR} for redder galaxies, except for the bluest β_{UV} , which give an IR peak strongly shifted to longer wavelengths. Blue galaxies are very faint on FIR, and we suggest that our FIR stacking analysis on LBG- $\beta 1$ is very uncertainty. Besides, if this IR behavior is real we should see it on LBG- $M\beta 1$ stacking analysis, and this is not happening.

The bottom left panel of Figures 4 illustrates the six SEDs and templates derived from the LBG- $M\beta 1$ stacking analysis. As a reminder, we split the sample into two large bins of M_* , and split each of these bins into three bins of β_{UV} . Their rest-frame FUV-to-NIR SEDs seem to subdivide into two different sets of templates, high and low M_* , with variations in the UV part of

the SED. No variations in the shape of the FIR part are found, except for an increase of the IR luminosity with M_* and β_{UV} . The bottom right panel of Figure 4 shows the ten SEDs and templates derived from the LBG- $M\beta 2$ stacking analysis. In this case, we split the sample in two large bins of β_{UV} , and each of them in five bins of M_* . Their rest-frame FUV-to-NIR SEDs present similar shapes in comparison with the stacking analysis as a function of M_* : an increase of the rest-frame NIR flux and a reddening of UV/optical part of the spectrum for massive LBGs. However, the split into β_{UV} , red and blue bins, gives access to two templates for each M_* , with similar NIR shapes, but in a strongly different UV part of the spectrum. The FIR shape does not present a large variety.

6. Dust attenuation

We analyzed in AM16 how the dust attenuation varies as a function of β_{UV} and M_* for our LBG sample by means of the IRX. At that time, we had access to the full FIR/submillimeter part of the spectrum to compute the average L_{IR} . However, the β_{UV} and M_* values associated with each stacked LBG SEDs were derived by averaging over the individual values of each LBG inside the stacked bin. The new rest-frame FUV-to-FIR stacking analysis allows us to derive the β_{UV} and M_* directly from the stacked LBG SEDs. We then reviewed the information in

the IRX- β_{UV} and IRX- M_* planes using the results obtained from the rest-frame FUV-to-FIR SED-fitting analysis on the stacked LBGs SEDs.

6.1. Dust attenuation as a function of β_{UV}

Figure 5 shows the IRX- β_{UV} plane, where we plot the results from our rest-frame FUV-to-FIR stacking analysis as a function of β_{UV} (LBG- β). This is compared with the well-known IRX- β_{UV} relation calibrated from local starburst galaxies (M99) and the relation recomputed by Takeuchi et al. (2012) using the same sample and new photometric data from AKARI and GALEX. We also include our previous IRX- β_{UV} relation derived from a FIR stacking analysis over the same LBG sample (AM16). In addition, we plot the IRX- β_{UV} results from LBGs at redshifts, $z \sim 3$ (Koprowski et al. 2018) and $2 < z < 3$ (Bouwens et al. 2016), star-forming galaxies at redshifts, $2 < z < 3$ (McLure et al. 2018) and $1.5 < z < 2.5$ (Reddy et al. 2018), and a mass selected sample at redshift $z \sim 3$ (Bourne et al. 2017).

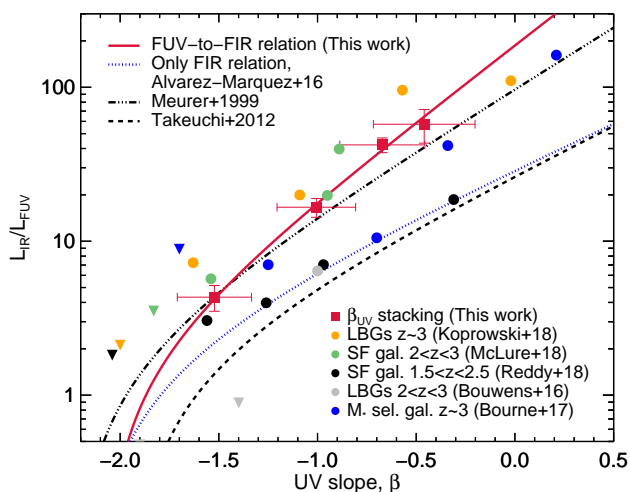


Fig. 5: IRX- β_{UV} diagram. Lines show different IRX- β_{UV} relations: the well-known local starburst galaxies calibration (M99; triple-dot-dashed line), the aperture correction of M99 relation by Takeuchi et al. (2012; dashed line), and the relation derived from a FIR stacking analysis over the same LBG sample (AM16; dotted blue line). In addition, we plot the IRX- β_{UV} results from LBGs at redshifts, $z \sim 3$ (Koprowski et al. 2018, orange dots) and $2 < z < 3$ (Bouwens et al. 2016, gray dots), star-forming galaxies at redshifts, $2 < z < 3$ (McLure et al. 2018, green dots) and $1.5 < z < 2.5$ (Reddy et al. 2018, black dots), and a mass selected sample at redshift $z \sim 3$ (Bourne et al. 2017, blue dots). The downward triangles represent upper limits.

The IRX- β_{UV} results from the FUV-to-FIR (this work) and only FIR (AM16) stacking analyses disagree, even if both are computed with the same LBG sample. The FUV-to-FIR results gives an IRX value that is ~ 2 - 3 times higher for a given β_{UV} than the FIR values. The difference resides on the method used to derive the β_{UV} in each of the analyses. In Appendix A, we demonstrate that $\beta_{UV-power}$ (AM16) are biased to redder values in comparison with β_{UV-SED} (this work, see Section 3.2). If the IRX- β_{UV} results from the FIR analysis are corrected by the relation between the $\beta_{UV-power}$ and β_{UV-SED} , obtained in Appendix A, they are in agreement with the IRX- β_{UV} relation obtained from the FUV-to-FIR analysis. Koprowski et al. (2018) have also

confirmed that discrepancies in the IRX- β_{UV} relation are due to bias in the method used to determine the β_{UV} . These authors suggested that these inconsistencies are driven by scatter in measured values of β_{UV} from limited photometry that serves to artificially flatten the IRX- β_{UV} relation. They obtained that the scatter is significantly reduced by determining β_{UV} from SED-fitting analysis, which is the same conclusion presented in Appendix A.

Our FUV-to-FIR stacking and SED-fitting analysis results as a function of β_{UV} follow the IRX- β_{UV} local relation (M99) within the uncertainties. These results are in agreement with previous stacking analyses done on star-forming galaxies at high- z . Magdis et al. (2010a) found that the dust-corrected UV-SFR derived from the M99 relation presents a good match with the FIR and radio SFR estimators for stacked IRAC spectropically confirmed LBGs at $z \sim 3$. Koprowski et al. (2018), by stacking a sample of ~ 4000 LBGs at redshifts, $3 < z < 5$, have concluded that LBGs are consistent with the M99 IRX- β_{UV} relation and do not present a redshift evolution. Similar results were obtained by McLure et al. (2018), who studied a sample of star-forming galaxies at redshifts, $2 < z < 3$, from a deep ALMA 1.3 mm continuum data. Additional stacking analysis of spectroscopically confirmed $z \sim 2$ LBGs in FIR (Reddy et al. 2012), $z \sim 4$ LBGs in the radio continuum (1.4GHz; To et al. 2014), and direct detections of LBGs in PACS at lower redshift ($z \sim 1$; Oteo et al. 2013b; Burgarella et al. 2011) also agree with the M99 relation. Bourne et al. (2017) have used a deconvolution methodology to reach below the confusion limit maps (SCUBA2 and Herschel) for massive galaxies at redshifts, $0.5 < z < 6$, detected in the CANDELS fields (AEGIS, COSMOS, and UDS). These authors have obtained similar results as for local starburst galaxies in M99, although their results deviate to higher IRX values at high stellar masses, which is similar to the analysis presented in Sect. 6.3. However, Reddy et al. (2018) have used ~ 3500 star-forming galaxies at redshifts, $1.5 < z < 2.5$, and have concluded that the M99 IRX- β_{UV} local relation overpredicts the IRX by a factor of ~ 3 at a given β_{UV} . Fujimoto et al. (2016) and Bouwens et al. (2016) used ALMA observations of LBGs at $z \sim 2$ - 3 , and also showed that the M99 relation overpredicts the IRX. The ALMA observations contain small samples that could make it difficult to constrain the IRX- β_{UV} relation statistically. In particular, Bouwens et al. (2016) stacked a LBG sample at $z = 2 - 3$ in bins of M_* and β_{UV} . Their results suggested an IRX- β_{UV} values below the M99 relation, but the high M_* bin ($\log(M_* [M_\odot]) > 9.75$) is in agreement within the uncertainties.

6.2. Dust attenuation as a function of M_*

Figure 6 shows the IRX- M_* plane, where the results from our rest-frame FUV-to-FIR stacking analysis as a function of M_* (LBG- M_*) are plotted. These are compared with the relationship presented by Bouwens et al. (2016) for star-forming galaxies at redshifts $2 < z < 3$ and defined from the combination of different works done in the literature (Reddy et al. 2010; Whitaker et al. 2014; Álvarez-Márquez et al. 2016). This relation includes that previously derived from a FIR stacking analysis over our LBG sample (AM16). We overplot the relations obtained from a stacking analysis of UV-selected galaxies at redshift $z \sim 3$ (Heinis et al. 2014) and a complete sample of star-forming galaxies up to $z \sim 4$ (Pannella et al. 2015). We also show the IRX- M_* results from LBGs at redshifts, $z \sim 3$ (Koprowski et al. 2018) and $2 < z < 3$ (Bouwens et al. 2016), and star-forming galaxies at redshifts, $2 < z < 3$ (McLure et al. 2018) and $1.5 < z < 2.5$ (Reddy et al. 2018). The IRX results from the FUV-to-FIR stack-

ing analysis show a good agreement at the highest stellar mass bins ($\log(M_* [M_\odot]) > 10$). However, the IRX results disagree at low stellar masses bins ($\log(M_* [M_\odot]) < 10$) presenting larger IRX values for a given M_* .

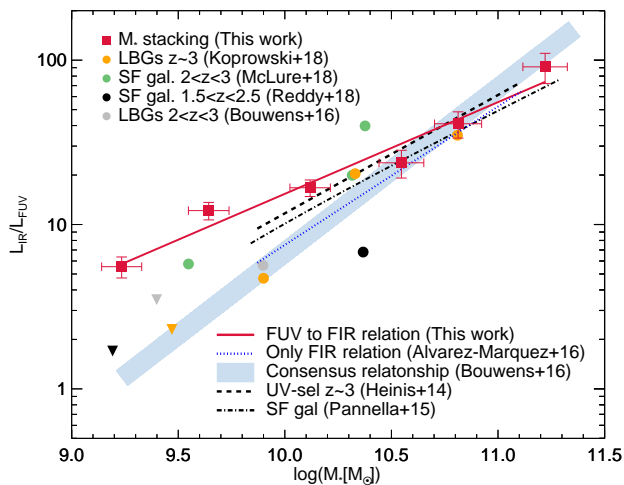


Fig. 6: IRX- M_* diagram. Our rest-frame FUV-to-FIR stacking analysis as a function of M_* (LBG- M) results and the power-law fit are shown by red squares and solid line. The blue line presents the consensus relationship for star-forming galaxies at redshifts $2 < z < 3$ (Bouwens et al. 2016), and defined by a combination of different works done in the literature (Reddy et al. 2010; Whitaker et al. 2014; Álvarez-Márquez et al. 2016). This relation includes that previously derived from a FIR stacking analysis over our LBG sample (AM16, dotted blue line). We overplot the relations obtained from a stacking analysis of UV-selected galaxies at redshift $z \sim 3$ (Heinis et al. 2014, dashed line) and a complete sample of star-forming galaxies up to $z \sim 4$ (Pannella et al. 2015, dot-dashed line). We also show the IRX- M_* results from LBGs at redshifts, $z \sim 3$ (Koprowski et al. 2018, orange dot) and $2 < z < 3$ (Bouwens et al. 2016, gray dot), and star-forming galaxies at redshifts $2 < z < 3$ (McLure et al. 2018, green dots) and $1.5 < z < 2.5$ (Reddy et al. 2018, black dots). The downward triangles represent upper limits.

We suggest that an incompleteness of our LBG sample in terms of M_* might be the origin of the IRX- M_* discrepancies. If M_* is proportional to the rest-frame NIR emission (Kauffmann & Charlot 1998), the incompleteness of our LBG sample at $z \sim 3$ in terms of M_* is proportional to the detectability of our LBGs at IRAC $3.6 \mu\text{m}$ observations. The mean fluxes of the LBG population with stellar masses, $\log(M_* [M_\odot]) < 10$, are between 1.2 to $3.6 \mu\text{Jy}$ (see Appendix C). Ilbert et al. (2010) showed that the i-band photometric redshift catalog (Ilbert et al. 2009, version 2.0), used to build our LBG sample in AM16 is 90% complete at $5 \mu\text{Jy}$ and 50% complete at $1 \mu\text{Jy}$ in the IRAC $3.6 \mu\text{m}$ observations. Then, the low stellar mass bins ($\log(M_* [M_\odot]) < 10$) of LBG- M stacking analysis are between 80% to 50% complete in term of M_* .

However, there are some indications in the literature that the origin of the departure might not be due to M_* bias. For instance, Whitaker et al. (2017) showed that the region corresponding to galaxies at $\log(M_* [M_\odot]) < 10$ and high IRX values is populated by galaxies. This effect does not seem to be at $z = 0$, however. It could also be noticed in Heinis et al. (2014) that there is a trend for galaxies with low- L_{UV} to have larger IRX. We can

wonder whether this effect does not hide the fact that these low- L_{UV} only trace dust-free stars in galaxies that might be otherwise dusty (meaning that most of the stars do not contribute to the UV luminosity). Finally, Spitler et al. (2014) studied a sample of 57 galaxies with $\log(M_* [M_\odot]) < 10.6$, and they find that massive star-forming galaxies can be found at all M_{UV} . So, we propose that the trend we observe at $\log(M_* [M_\odot]) < 10$ in Figure 6 might be real and not due to an observational bias. The impact of this hypothesis will be further studied in Bogdanoska et al. (in prep.). In Section 6.3, when LBGs are stacked as a function of M_* and β_{UV} , a population of LBGs appear to locate at the same region of the IRX- M_* diagram than Whitaker et al. (2017). If this population is removed to perform the stacking analysis and derive the mean IRX- M_* relation (light red filled square in Figure 8), the results are closer to the IRX- M_* relations from Pannella et al. (2015) and Heinis et al. (2014), and the star-forming galaxies at $2 < z < 3$ stacked in ALMA observation (McLure et al. 2018).

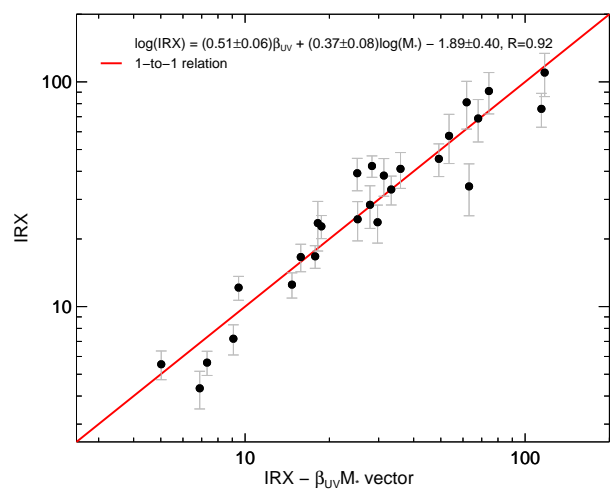


Fig. 7: Empirical IRX calibration by combination the β_{UV} and M_* . The plane fit in the 3D IRX- β_{UV} - M_* diagram provides us with the equation $\log(\text{IRX}) = (0.51 \pm 0.06)\beta_{\text{UV}} + (0.37 \pm 0.08)\log(M_* [M_\odot]) - 1.89 \pm 0.40$, which can be used to correct the dust attenuation when β_{UV} and M_* are known. The y-axis corresponds to the IRX obtained from SED-fitting analysis over the stacked LBGs SEDs. The x-axis corresponds to the IRX calculated from the plane fit equation. The black points indicate the results from the SED-fitting and stacking analysis as a function of β_{UV} and M_* , and the combination of the two (LBG- β , LBG- M , LBG- $M\beta 1$, and LBG- $M\beta 2$). The red line indicates the 1-to-1 relation.

6.3. Dispersion on the IRX- M_* and IRX- β_{UV} planes

We use our stacking analyses (LBG- $M\beta$) to investigate the dispersion on the IRX- β_{UV} and IRX- M_* planes, and the validity of the IRX- β_{UV} and IRX- M_* mean relations. On the LBG- $M\beta$ stacking analyses, the LBG sample is split on the (M_*, β_{UV}) plane in two different ways. For LBG- $M\beta 1$, the LBG sample is divided into two bins of M_* , and each of these is split as a function of β_{UV} . And for LBG- $M\beta 2$, it is divided into two bins of β_{UV} and each of these is split as a function of M_* . Figure 8 shows the results from the LBG- $M\beta$ stacking analyses in the IRX- β_{UV} and IRX- M_* planes. The results suggest large dispersion on both planes, as a consequence of the M_* evolution in

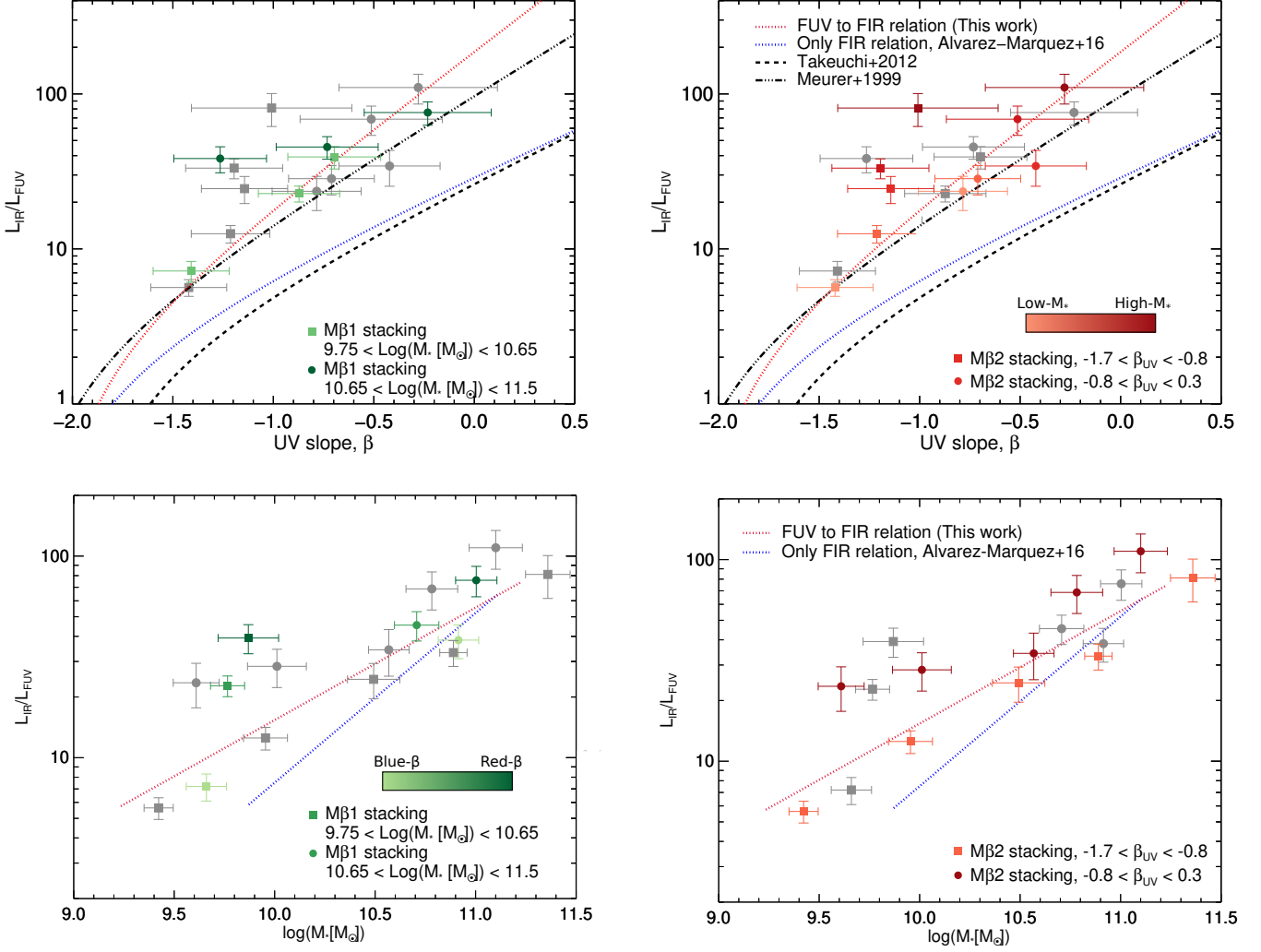


Fig. 8: LBG- $M\beta 1$ and LBG- $M\beta 2$ results in the IRX- β_{UV} (top panels) and IRX- M_* (bottom panels) planes. Top left panel: the LBG- $M\beta 1$ are shown in green; the tonalities represent the two different bins in M_* , $9.75 < \log(M_* [M_\odot]) < 10.65$ (light green filled square) and $10.65 < \log(M_* [M_\odot]) < 11.5$ (dark green filled circles). Top right panel: the LBG- $M\beta 2$ results are shown in red; the tonalities represent the increase of the M_* from 9.75 (light red) to 11.50 (dark red). The filled squares represent the bluer β_{UV} bin and the filled circles the redder β_{UV} bin. Bottom left panel: LBG- $M\beta 1$ are shown in green; the tonalities represent the increase of the β_{UV} from -1.7 (light green) to 0.5 (dark green). The filled squares represent the low M_* bin and the filled circles the high M_* bin. Bottom right panel: The LBG- $M\beta 2$ results are shown in red; the tonalities represent the two different bins in β_{UV} , $-1.7 < \beta_{UV} < -0.8$ (light red filled square) and $-0.8 < \beta_{UV} < 0.3$ (dark red filled circles). The gray points in all diagrams represent the LBG- $M\beta$ results that are not highlighted in color.

the IRX- β_{UV} plane and the β_{UV} in the IRX- M_* plane. On the one hand, high stellar mass LBGs present higher IRX values than the mean IRX- β_{UV} relation. Similar results were reported by Bourne et al. (2017) in the IRX- β_{UV} plane. These authors showed an evolution of the IRX- β_{UV} relation from low to high stellar masses using a sample of massive galaxies at redshifts $0.5 < z < 6$. Some studies of IR-selected galaxy samples have found IRX- β_{UV} values located above M99 relation (Casey et al. 2014; Oteo et al. 2013a; Buat et al. 2015), which suggest that the criterion to select the sample has a strong impact on the mean dust attenuation of a galaxy population. On the other hand, redder LBGs tend to have higher IRX values than the mean IRX- M_* relation. In particular, a population of LBGs with $\beta_{UV} < -1$ and stellar masses ($\log(M_* [M_\odot]) < 10$) shows large IRX values that flatten the mean IRX- M_* presented in Figure 6.

The dependence of M_* in the IRX- β_{UV} plane and β_{UV} in the IRX- M_* plane makes us think about the utility and efficiency of providing a new empirical IRX relation combining the β_{UV} and M_* . It may reduce the uncertainty to derive the dust attenuation for galaxies for which only UV/optical/NIR observations are available. We use the results from the SED-fitting and stacking analysis as a function of β_{UV} and M_* , and the combination of the two (LBG- β , LBG- M , LBG- $M\beta 1$, and LBG- $M\beta 2$) to attempt performing a plane fit in the 3D IRX- β_{UV} - M_* diagram. We obtain a mean relation equal to $\log(IRX) = (0.51 \pm 0.06)\beta_{UV} + (0.37 \pm 0.08)\log(M_* [M_\odot]) - 1.89 \pm 0.40$. Figure 7 shows the dispersion between the IRX of each stacked LBGs obtained from SED-fitting analysis, and the IRX derived from the mean IRX- β_{UV} - M_* relation.

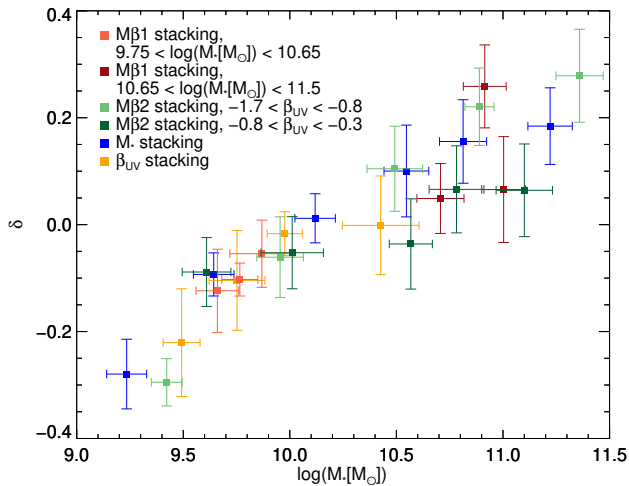


Fig. 9: Change of the slope of the dust attenuation law with respect to Calzetti (δ) as a function of stellar mass. The different colors show each stacking analysis as a function of β_{UV} and M_* , and the combination of both parameters (LBG- β , LBG- M , LBG- $M\beta1$, and LBG- $M\beta2$). This suggests a correlation between the stellar mass of a galaxy and the shape of the dust attenuation curve, which is steeper for LBGs with $\log(M_*[M_\odot]) < 10.25$ and grayer for LBGs with $\log(M_*[M_\odot]) > 10.25$ than Calzetti’s law.

6.4. Shape of the dust attenuation curve for LBGs at $z \sim 3$

The Calzetti law is frequently assumed when studying star-forming galaxies at high- z (e.g., Bouwens et al. 2009; Schaerer et al. 2013; Finkelstein et al. 2015). From observations in the local universe, it is well known that dust attenuation curves are not universal across galaxies. Most sight lines in the Milky Way (MW) have a strong extinction bump near 2175 Å (Stecher 1965; Cardelli et al. 1989). However, the feature is weaker in the Large Magellanic Cloud (LMC; Koornneef & Code 1981) and absent in the Small Magellanic Cloud (SMC; Prevot et al. 1984). This diversity is also reflected by systematic changes in the FUV slope, which gets steeper from MW to SMC. Calzetti et al. (1994) deduced a mean dust attenuation curve from a sample of 39 local UV-bright starburst galaxies. Their measurements are characterized by a grayer FUV slope than both MW and LMC extinction curves and an absence of the 2175 Å absorption feature. At higher redshifts, a variety can be also seen. Buat et al. (2011b, 2012) found for a UV-selected galaxy at $z > 1$ a clear present of 2175 Å bump and evidence for a steeper rise of the dust attenuation curve in comparison to the Calzetti law. Other studies support this model, demonstrating that the 2175 Å bump is typically visible in normal star-forming galaxies (e.g., Burgarella et al. 2005; Noll et al. 2007; Conroy 2010). Other authors have also suggested that dust attenuation curves vary significantly at any redshift (e.g., Kriek & Conroy 2013; Zeimann et al. 2015; Salmon et al. 2016; Lo Faro et al. 2017). This diversity in the shape of the dust attenuation curves could be produced by the differences in the dust grain properties, the relative geometrical distribution of stars and dust within a galaxy, the line-of-sight galaxy orientation, and the galaxy type (Witt & Gordon 2000b; Pierini et al. 2004; Tuffs et al. 2004; Chevillard et al. 2013).

The results from the SED-fitting analysis over our stacked LBGs SEDs suggest a large variation in the shape of the dust

attenuation curve across the LBG population at $z \sim 3$. We obtain a range of δ ’s from -0.3 to 0.3 (see Appendix D), which produce dust attenuation curves steeper and grayer than Calzetti law ($\delta = 0$), respectively. Similar results were reported by Salmon et al. (2016), who found a range of δ ’s from -0.5 to 0.2 in star-forming galaxies at $z \sim 1.5 - 3$. Figure 9 illustrates the dependence of δ as a function of M_* for the stacking analysis as a function of β_{UV} and M_* , and the combination of these both parameters (LBG- β , LBG- M , LBG- $M\beta1$, and LBG- $M\beta2$). We obtain that δ is well correlated with the M_* . The low stellar mass population of LBGs ($\log(M_*[M_\odot]) < 10.25$) favors steeper dust attenuation curves than the Calzetti’s law, and the large stellar mass population of LBGs ($\log(M_*[M_\odot]) > 10.25$) favors grayer Calzetti’s law. A similar trend with the stellar mass is seen in the local Universe by Salim et al. (2018); these authors have suggested that the apparent dependence with the stellar mass is due to a relation between the stellar mass and optical opacity. They conclude that opaque galaxies have shallower dust attenuation laws. Cullen et al. (2018) studied a sample of star-forming galaxies at redshifts, $3 < z < 4$, and stellar mass range, $8.2 < \log(M_*[M_\odot]) < 10.6$. Their mean FUV-to-optical dust attenuation curve is in agreement with Calzetti’s, and gets steeper at lower masses. However, Zeimann et al. (2015) performed an analysis of star-forming galaxies selected by their rest-frame optical emission lines at redshifts, $1.9 < z < 2.35$, and mass range, $7.2 < \log(M_*[M_\odot]) < 10.2$. They found grayer dust attenuation curves than Calzetti’s, which differs from our findings.

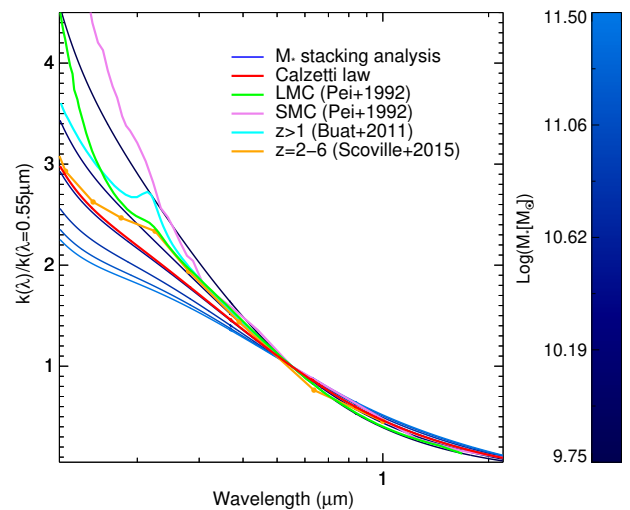


Fig. 10: Dust attenuation curves derived from the SED-fitting analysis over the stacked LBGs SEDs obtained from the stacking analysis as a function of M_* . These curves are color coded as a function of M_* : light blue represents larger stellar masses which are grayer than Calzetti’s law (red line), and dark blue corresponds to lower stellar masses which are steeper than Calzetti’s law. As a comparison, we also show the LMC and SMC dust extinction curve (Pei 1992) and two additional attenuation curves derived from UV-selected galaxies at $z > 1$ (Buat et al. 2011b) and star-forming galaxies at $z \sim 2$ to 6 (Scoville et al. 2015).

Figure 10 illustrates the derived dust attenuation curves in the stacked LBGs SEDs as a function of M_* (LBG- M). This figure shows how dust attenuation curves get steeper when the stellar mass decreases, up to the lowest stellar mass bin that presents a slope closer to the SMC dust attenuation curve (Pei 1992). Other mean dust attenuation laws derived from UV-selected galaxies at

$z > 1$ (Buat et al. 2011b) and star-forming galaxies at $z \sim 2$ to 6 in the COSMOS field (Scoville et al. 2015) are also compared; they are in agreement with the derived dust attenuation curves for our stacked LBGs SEDs.

We note in our stacked LBGs SEDs that some of the z-band ($\lambda_{rest} \sim 2200\text{\AA}$) data points have lower observed flux than its consecutive data points (i-band and Y-band). This might be a consequence of a larger dust attenuation owing to the coincidence with the UV bump at 2175\AA . As we commented in Section 5.1, the spectral resolution of the FUV-to-FIR stacked LBGs SEDs is not sufficient to constrain the amplitude and shape of the UV bump, and its amplitude has been set to zero in our SED-fitting analysis. However, the presence or not of a UV bump in the dust attenuation law might modify the derived δ values. We performe an additional SED-fitting analysis with the amplitude of the UV bump as a free parameter to check the validity of the derived δ values. We obtain a mean differences, $\langle \delta_{D_{\lambda_0, \gamma, E_{bump} - free}} - \delta_{D_{\lambda_0, \gamma, E_{bump} = 0}} \rangle = -0.013 \pm 0.008$, which are within the derived δ 's uncertainties of the initial SED-fitting analysis.

6.5. IRX- β_{UV} plane and the slope of the dust attenuation curve

We previously reported a large dispersion in the IRX- β_{UV} plane associated with a M_* variations. We also obtain a diversity of dust attenuation curves along our LBG sample, which correlates with the M_* . We check in this section if the dispersion on the IRX- β_{UV} plane is a consequence of a variety in M_* or in the shape of the dust attenuation curve. A few recent studies showed that the diversity in the shape of the dust attenuation curves has a strong impact on shaping the IRX- β_{UV} plane (e.g., Salmon et al. 2016; Lo Faro et al. 2017).

(e.g., SFH, metallicity, and dust attenuation law). If we focus on the dust attenuation law and fix the others properties, when the UV shape of the dust attenuation curve changes the observed UV part of the spectrum would consequently be modified along with its associated β_{UV} . To test this, we use CIGALE in its *SED-modeling* mode to compute synthetic SEDs with a fixed configuration (delayed-SFH with $\tau=100\text{Myr}$ and age = 300Myr , metallicity = $0.02Z_{\odot}$, and fixed IR model), and different dust attenuation laws ($-0.4 < \delta < 0.4$) and reddening ($0 < E(B-V) < 1.5$).

Figure 11 illustrates the IRX- β_{UV} plane color coded as a function of δ . The continuous lines represent the simulations performed with CIGALE for the different δ values. Dust attenuation curves steeper than the Calzetti's law, with $\delta < 0$, are **located** below the M99 relation, and dust attenuation curves grayer than Calzetti's law, with $\delta > 0$, are located above. We note that the IRX- β_{UV} relations simulated for each δ are not unique as we show in this work. This is a consequence of fixing the metallicities and SFH. These relations should be broader if we consider different SFHs and metallicities, as in Salmon et al. (2016) and Lo Faro et al. (2017). We overplot the results from the SED-fitting and stacking analysis as functions of β_{UV} and M_* and the combination of both parameters (LBG- β , LBG- M , LBG- $M\beta 1$, and LBG- $M\beta 2$). Taking into account the uncertainties in the SFH and metallicity, our stacked LBGs are in agreement with our simulations. Our stacked LBGs with associated $\delta \sim 0$ follow M99, and when δ increases the objects present bluer β_{UV} and higher IRX values than M99 relation. We conclude that dust attenuation curves are one of the main drivers that shapes the IRX- β_{UV} plane, following previous studies in other galaxy population (e.g., Salmon et al. 2016; Lo Faro et al. 2017; Salim & Boquien 2019).

7. Summary and conclusions

We investigate the full rest-frame FUV-to-FIR emission of LBGs at $z \sim 3$ by stacking analysis at the optical (*BVRiz* bands), NIR (*YJHKs* bands), IRAC (3.6, 4.5, 5.6 and $8.0\ \mu\text{m}$), MIPS ($24\ \mu\text{m}$), PACS (100 and $160\ \mu\text{m}$), SPIRE (250, 350, and $500\ \mu\text{m}$), and AzTEC (1.1mm) observations. We use a subsample of ~ 17000 LBGs from those previously selected and characterized in AM16. We split our LBG sample as a function of the single parameters L_{FUV} , β_{UV} , and M_* , and the combination of both β_{UV} and M_* in the (β_{UV}, M_*) plane. This allows us to build 30 rest-frame FUV-to-FIR LBGs SEDs at $z \sim 3$ and investigate the evolution of their physical properties as a function of the binning parameters.

We use CIGALE, a physically oriented spectral synthesis and SED-fitting code, to analyze our rest-frame FUV-to-FIR stacked LBGs SEDs. The CIGALE code provides us with the synthetic model spectra that better fit our stacked LBGs SEDs by χ^2 minimization and the mean physical parameters that characterize each of the stacked LBG SEDs by applying a Bayesian analysis. After performing exhaustive checks on the validity of the derived physical parameters, we conclude that the SED-fitting analysis can derive fully consistent physical parameters, i.e., M_* , L_{IR} , A_{FUV} , SFR, and change of the slope of the dust attenuation law with respect to Calzetti - δ .

We use the stacked LBGs SEDs and their associated modeled spectra to build a library of 30 SEDs and templates of LBGs at $z \sim 3$. Thanks to the binning configuration used to perform the stacking analysis, we derive a set of templates with a large variety of physical properties. The library contains templates within an interval of stellar mass, $9.2 < \log(M_* [M_{\odot}]) < 11.4$, SFR, $20 < SFR [M_{\odot} \text{yr}^{-1}] < 300$, β_{UV} , $-1.8 < \beta_{UV} < -0.2$,

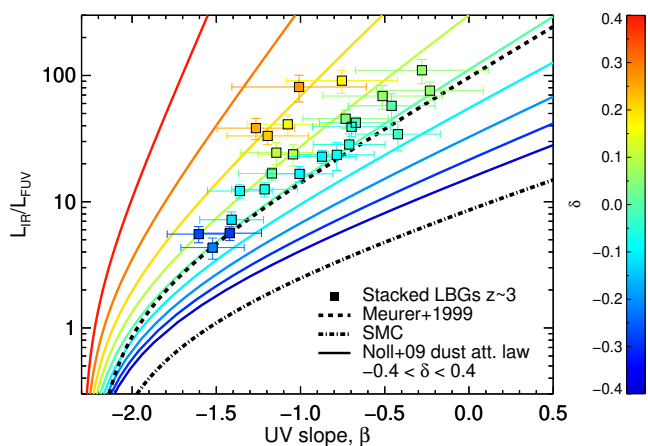


Fig. 11: IRX- β_{UV} diagram seeing from a δ point of view. Continuous lines show the simulation performed by CIGALE with a fixed SFH and metallicity for different dust attenuation curves (see text). The square points represent the results from the SED-fitting analysis and stacking analysis as a function of β_{UV} and M_* , and the combination of the two (LBG- β , LBG- M , LBG- $M\beta 1$, and LBG- $M\beta 2$). Both are color coded as a function δ . The dashed and dot-dashed lines represent the classical M99 and SMC (Bouwens et al. 2016) relations, respectively

The observed UV part of the spectrum, where the β_{UV} is calculated, depends on different physical properties of a galaxy

FUV dust attenuation, $1.5 < A_{\text{FUV}} [\text{mag}] < 4.8$, IR luminosity, $11.2 < \log(L_{\text{IR}} [L_{\odot}]) < 12.7$, and FUV luminosity, $10.4 < \log(L_{\text{FUV}} [L_{\odot}]) < 11.2$. This diversity makes our library very versatile in the sense that our templates fit the physical properties of a large population of star-forming galaxies at $z \sim 3$.

We use the so-called IRX and the mean physical parameters derived for each of the rest-frame FUV-to-FIR stacked SEDs to investigate the dust attenuation properties of LBGs at $z \sim 3$. We conclude as follow:

- Our LBG sample follows the well-known IRX- β_{UV} calibration from local starburst galaxies (M99), when LBGs are stacked as a function of β_{UV} (LBG- β), which is in agreement with recent works done on star-forming galaxies at high- z (Koprowski et al. 2018; McLure et al. 2018; Bourne et al. 2017).
- Our LBG sample, stacked as a function of M_* (LBG- M), is in agreement with most of the IRX- M_* relations presented in the literature at high stellar masses ($\log(M_* [M_{\odot}]) > 10$, Pannella et al. 2015; Heinis et al. 2014; Bouwens et al. 2016; Álvarez-Márquez et al. 2016). However, it provides higher IRX values for a given M_* at low stellar masses ($\log(M_* [M_{\odot}]) < 10$).
- If our LBG sample is stacked as a function of a combination of both M_* and β_{UV} (LBG- $M\beta 1$ and LBG- $M\beta 2$), the sample shows a large dispersion on the IRX- M_* and IRX- β_{UV} planes. We find that the evolution to higher M_* or redder β_{UV} makes them differ from the main IRX- M_* and IRX- β_{UV} relations. New empirical IRX relation combining β_{UV} and M_* is suggested.

Finally, we investigate which dust attenuation curve is more likely to reproduce our LBG sample. We use Noll et al. (2009) dust attenuation law recipe and derive a variation of δ (change in the slope of the dust attenuation law with respect to Calzetti's law) from -0.3 to 0.3, which is well correlated with M_* . Steeper dust attenuation curves than Calzetti's are favored in low stellar mass LBGs ($\log(M_* [M_{\odot}]) < 10.25$), while grayer dust attenuation curves than Calzetti's are favored in high stellar mass LBGs ($\log(M_* [M_{\odot}]) > 10.25$). Combining **the simulation and stacked** results from our LBG sample, we corroborate that the slope of the dust attenuation curve is one of the main drivers to shape the IRX- β_{UV} plane.

Acknowledgements. JAM acknowledges support from the Spanish Ministry of Science, Innovation and Universities through project number ESP2017-83197. We gratefully acknowledge the contributions of the entire COSMOS collaboration consisting of more than 100 scientists. This work makes use of TOPCAT (<http://www.star.bristol.ac.uk/~mbt/topcat/>).

References

Álvarez-Márquez, J., Burgarella, D., Heinis, S., et al. 2016, *A&A*, 587, A122
 Baugh, C. M., Lacey, C. G., Frenk, C. S., et al. 2005, *MNRAS*, 356, 1191
 Bertin, E. & Arnouts, S. 1996, *A&AS*, 117, 393
 Béthermin, M., Dole, H., Beelen, A., & Aussel, H. 2010, *A&A*, 512, A78
 Béthermin, M., Le Floch, E., Ilbert, O., et al. 2012, *A&A*, 542, A58
 Bian, F., Fan, X., Jiang, L., et al. 2013, *ApJ*, 774, 28
 Blaizot, J., Guiderdoni, B., Devriendt, J. E. G., et al. 2004, *MNRAS*, 352, 571
 Boquien, M., Burgarella, D., Roehlly, Y., et al. 2019, *A&A*, 622, A103
 Bourne, N., Dunlop, J. S., Merlin, E., et al. 2017, *MNRAS*, 467, 1360
 Bouwens, R. J., Aravena, M., Decarli, R., et al. 2016, *ApJ*, 833, 72
 Bouwens, R. J., Illingworth, G. D., Franx, M., et al. 2009, *ApJ*, 705, 936
 Bouwens, R. J., Illingworth, G. D., Oesch, P. A., et al. 2015, *ApJ*, 803, 34
 Bruzual, G. & Charlot, S. 2003, *MNRAS*, 344, 1000
 Buat, V., Giovannoli, E., Heinis, S., et al. 2011a, *A&A*, 533, A93
 Buat, V., Giovannoli, E., Heinis, S., et al. 2011b, *A&A*, 533, A93
 Buat, V., Heinis, S., Boquien, M., et al. 2014, *A&A*, 561, A39

Buat, V., Noll, S., Burgarella, D., et al. 2012, *A&A*, 545, A141
 Buat, V., Oi, N., Heinis, S., et al. 2015, *A&A*, 577, A141
 Burgarella, D., Buat, V., Gruppioni, C., et al. 2013, *A&A*, 554, A70
 Burgarella, D., Buat, V., & Iglesias-Páramo, J. 2005, *MNRAS*, 360, 1413
 Burgarella, D., Heinis, S., Magdis, G., et al. 2011, *ApJ*, 734, L12
 Calzetti, D., Armus, L., Bohlin, R. C., et al. 2000, *ApJ*, 533, 682
 Calzetti, D., Kinney, A. L., & Storchi-Bergmann, T. 1994, *ApJ*, 429, 582
 Capak, P., Aussel, H., Ajiki, M., et al. 2007, *ApJS*, 172, 99
 Capak, P. L., Carilli, C., Jones, G., et al. 2015, *Nature*, 522, 455
 Cardelli, J. A., Clayton, G. C., & Mathis, J. S. 1989, *ApJ*, 345, 245
 Casey, C. M., Berta, S., Béthermin, M., et al. 2012, *ApJ*, 761, 140
 Casey, C. M., Scoville, N. Z., Sanders, D. B., et al. 2014, *ApJ*, 796, 95
 Castellano, M., Sommariva, V., Fontana, A., et al. 2014, *A&A*, 566, A19
 Chabrier, G. 2001, *ApJ*, 554, 1274
 Chabrier, G. 2003, *ApJ*, 586, L133
 Chapman, S. C. & Casey, C. M. 2009, *MNRAS*, 398, 1615
 Chevallard, J., Charlot, S., Wandelt, B., & Wild, V. 2013, *MNRAS*, 432, 2061
 Ciesla, L., Charmandaris, V., Georgakakis, A., et al. 2015, *A&A*, 576, A10
 Conroy, C. 2010, *MNRAS*, 404, 247
 Coppin, K. E. K., Geach, J. E., Almaini, O., et al. 2015, *MNRAS*, 446, 1293
 Cullen, F., McLure, R. J., Khochfar, S., et al. 2018, *MNRAS*, 476, 3218
 Dole, H., Lagache, G., Puget, J.-L., et al. 2006, *A&A*, 451, 417
 Draine, B. T. & Li, A. 2007, *ApJ*, 657, 810
 Finkelstein, S. L., Papovich, C., Salmon, B., et al. 2012, *ApJ*, 756, 164
 Finkelstein, S. L., Ryan, Jr., R. E., Papovich, C., et al. 2015, *ApJ*, 810, 71
 Fudamoto, Y., Ivison, R. J., Oteo, I., et al. 2017a, *MNRAS*, 472, 2028
 Fudamoto, Y., Oesch, P. A., Schinnerer, E., et al. 2017b, *MNRAS*, 472, 483
 Fujimoto, S., Ouchi, M., Ono, Y., et al. 2016, *ApJS*, 222, 1
 Gialavisco, M. 2002, *ARA&A*, 40, 579
 Griffin, M. J., Abergel, A., Abreu, A., et al. 2010, *A&A*, 518, L3
 Heinis, S., Buat, V., Béthermin, M., et al. 2013, *MNRAS*, 429, 1113
 Heinis, S., Buat, V., Béthermin, M., et al. 2014, *MNRAS*, 437, 1268
 Ilbert, O., Capak, P., Salvato, M., et al. 2009, *ApJ*, 690, 1236
 Ilbert, O., Salvato, M., Le Floch, E., et al. 2010, *ApJ*, 709, 644
 Kauffmann, G. & Charlot, S. 1998, *MNRAS*, 297, L23
 Koornneef, J. & Code, A. D. 1981, *ApJ*, 247, 860
 Koprowski, M. P., Coppin, K. E. K., Geach, J. E., et al. 2018, *MNRAS*, 479, 4355
 Kriek, M. & Conroy, C. 2013, *ApJ*, 775, L16
 Kroupa, P. 2001, *MNRAS*, 322, 231
 Laigle, C., McCracken, H. J., Ilbert, O., et al. 2016, *ApJS*, 224, 24
 Lee, S.-K., Ferguson, H. C., Somerville, R. S., Wiklind, T., & Gialavisco, M. 2010, *ApJ*, 725, 1644
 Lo Faro, B., Buat, V., Roehlly, Y., et al. 2017, *MNRAS*, 472, 1372
 Lo Faro, B., Monaco, P., Vanzella, E., et al. 2009, *MNRAS*, 399, 827
 López Fernández, R., Cid Fernandes, R., González Delgado, R. M., et al. 2016, *MNRAS*, 458, 184
 Lutz, D., Poglitsch, A., Altieri, B., et al. 2011, *A&A*, 532, A90
 Madau, P. & Dickinson, M. 2014, *ARA&A*, 52, 415
 Madau, P., Ferguson, H. C., Dickinson, M. E., et al. 1996, *MNRAS*, 283, 1388
 Magdis, G. E., Daddi, E., Béthermin, M., et al. 2012, *ApJ*, 760, 6
 Magdis, G. E., Elbaz, D., Daddi, E., et al. 2010a, *ApJ*, 714, 1740
 Magdis, G. E., Elbaz, D., Hwang, H. S., et al. 2010b, *ApJ*, 720, L185
 Magdis, G. E., Rigopoulou, D., Huang, J.-S., & Fazio, G. G. 2010c, *MNRAS*, 401, 1521
 Magdis, G. E., Rigopoulou, D., Huang, J.-S., et al. 2008, *MNRAS*, 386, 11
 Mannucci, F., Cresci, G., Maiolino, R., et al. 2009, *MNRAS*, 398, 1915
 Maraston, C., Pforr, J., Renzini, A., et al. 2010, *MNRAS*, 407, 830
 Marsden, G., Ade, P. A. R., Bock, J. J., et al. 2009, *ApJ*, 707, 1729
 McCracken, H. J., Milvang-Jensen, B., Dunlop, J., et al. 2012, *A&A*, 544, A156
 McLure, R. J., Dunlop, J. S., Cullen, F., et al. 2018, *MNRAS*, 476, 3991
 Meurer, G. R., Heckman, T. M., & Calzetti, D. 1999, *ApJ*, 521, 64
 Nguyen, H. T., Schulz, B., Levenson, L., et al. 2010, *A&A*, 518, L5
 Noll, S., Burgarella, D., Giovannoli, E., et al. 2009, *A&A*, 507, 1793
 Noll, S., Pierini, D., Pannella, M., & Savaglio, S. 2007, *A&A*, 472, 455
 Oesch, P. A., Bouwens, R. J., Illingworth, G. D., et al. 2015, *ApJ*, 808, 104
 Oesch, P. A., Bouwens, R. J., Illingworth, G. D., Labbé, I., & Stefanon, M. 2018, *ApJ*, 855, 105
 Oliver, S. J., Bock, J., Altieri, B., et al. 2012, *MNRAS*, 424, 1614
 Oteo, I., Cepa, J., Bongiovanni, A., et al. 2013a, *A&A*, 554, L3
 Oteo, I., Magdis, G., Bongiovanni, A., et al. 2013b, *MNRAS*, 435, 158
 Pannella, M., Elbaz, D., Daddi, E., et al. 2015, *The Astrophysical Journal*, 807, 141
 Papovich, C., Dickinson, M., & Ferguson, H. C. 2001, *ApJ*, 559, 620
 Pei, Y. C. 1992, *ApJ*, 395, 130
 Pentericci, L., Grazian, A., Scarlata, C., et al. 2010, *A&A*, 514, A64
 Pforr, J., Maraston, C., & Tonini, C. 2012, *MNRAS*, 422, 3285
 Pierini, D., Gordon, K. D., Witt, A. N., & Madsen, G. J. 2004, *ApJ*, 617, 1022
 Pilbratt, G. L., Riedinger, J. R., Passvogel, T., et al. 2010, *A&A*, 518, L1
 Poglitsch, A., Waelkens, C., Geis, N., et al. 2010, *A&A*, 518, L2

- Prevot, M. L., Lequeux, J., Prevot, L., Maurice, E., & Rocca-Volmerange, B. 1984, A&A, 132, 389
- Reddy, N., Dickinson, M., Elbaz, D., et al. 2012, ApJ, 744, 154
- Reddy, N. A., Erb, D. K., Pettini, M., Steidel, C. C., & Shapley, A. E. 2010, ApJ, 712, 1070
- Reddy, N. A., Kriek, M., Shapley, A. E., et al. 2015, ApJ, 806, 259
- Reddy, N. A., Oesch, P. A., Bouwens, R. J., et al. 2018, ApJ, 853, 56
- Rigopoulou, D., Magdis, G., Ivison, R. J., et al. 2010, MNRAS, 409, L7
- Roberts-Borsani, G. W., Bouwens, R. J., Oesch, P. A., et al. 2016, ApJ, 823, 143
- Salim, S. & Boquien, M. 2019, ApJ, 872, 23
- Salim, S., Boquien, M., & Lee, J. C. 2018, ApJ, 859, 11
- Salmon, B., Papovich, C., Long, J., et al. 2016, ApJ, 827, 20
- Salpeter, E. E. 1955, ApJ, 121, 161
- Sanders, D. B., Salvato, M., Aussel, H., et al. 2007, ApJS, 172, 86
- Schaerer, D., de Barros, S., & Sklias, P. 2013, A&A, 549, A4
- Scoville, N., Aussel, H., Brusa, M., et al. 2007, ApJS, 172, 1
- Scoville, N., Faisst, A., Capak, P., et al. 2015, ApJ, 800, 108
- Shapley, A. E., Steidel, C. C., Adelberger, K. L., et al. 2001, ApJ, 562, 95
- Shapley, A. E., Steidel, C. C., Erb, D. K., et al. 2005, ApJ, 626, 698
- Somerville, R. S., Primack, J. R., & Faber, S. M. 2001, MNRAS, 320, 504
- Spitler, L. R., Straatman, C. M. S., Labbé, I., et al. 2014, ApJ, 787, L36
- Stark, D. P., Ellis, R. S., Bunker, A., et al. 2009, ApJ, 697, 1493
- Stecher, T. P. 1965, ApJ, 142, 1683
- Stefanon, M., Labbé, I., Bouwens, R. J., et al. 2017, ApJ, 851, 43
- Steidel, C. C., Giavalisco, M., Dickinson, M., & Adelberger, K. L. 1996, AJ, 112, 352
- Takeuchi, T. T., Yuan, F.-T., Ikeyama, A., Murata, K. L., & Inoue, A. K. 2012, ApJ, 755, 144
- Taniguchi, Y., Kajisawa, M., Kobayashi, M. A. R., et al. 2015, PASJ, 67, 104
- Taniguchi, Y., Scoville, N., Murayama, T., et al. 2007, ApJS, 172, 9
- To, C.-H., Wang, W.-H., & Owen, F. N. 2014, ApJ, 792, 139
- Tuffs, R. J., Popescu, C. C., Völk, H. J., Kylafis, N. D., & Dopita, M. A. 2004, A&A, 419, 821
- Verma, A., Lehnert, M. D., Förster Schreiber, N. M., Bremer, M. N., & Douglas, L. 2007, MNRAS, 377, 1024
- Viero, M. P., Moncelsi, L., Quadri, R. F., et al. 2013, ApJ, 779, 32
- Whitaker, K. E., Franx, M., Leja, J., et al. 2014, ApJ, 795, 104
- Whitaker, K. E., Pope, A., Cybulski, R., et al. 2017, ApJ, 850, 208
- Witt, A. N. & Gordon, K. D. 2000a, ApJ, 528, 799
- Witt, A. N. & Gordon, K. D. 2000b, ApJ, 528, 799
- Zeimann, G. R., Ciardullo, R., Gronwall, C., et al. 2015, ApJ, 814, 162

Appendix A: Comparison of methods to derive the β_{UV} on our LBG sample

We find a large discrepancy between the β_{UV} calculations from Section 3.2 and those presented by AM16 on the same LBG sample. Both methodologies use the same wavelength interval to perform the power-law fit. However, in Section 3.2, we use the best-fit synthetic spectral model obtained on the rest-frame UV-to-optical SED-fitting analysis (β_{UV-SED}), and the rest-frame UV photometry in AM16 ($\beta_{UV-Power}$). Figure A.1 shows, in red, the comparison between $\beta_{UV-Power}$ (y-axis) and β_{UV-SED} (x-axis) for each LBG of the sample. This figure illustrates that the $\beta_{UV-Power}$ are redder than the β_{UV-SED} in the range of β_{UV} used in that work ($1.9 < \beta_{UV} < 0.3$) and that their differences increase at redder values.

Finkelstein et al. (2012) used a sample of $z = 4$ to 8 galaxies selected in CANDELS fields to compare the β_{UV-SED} and $\beta_{UV-Power}$. They found that the results from the SED-fitting method presents essentially no bias at all redshifts, while the results from power-law method are biased toward redder values. Reddy et al. (2015) used a sample of $z \sim 2$ star-forming galaxies to compare the two different β_{UV} calculations, concluding that the two measurements are highly correlated. However, Table 2 of their paper shows that the mean values of $\beta_{UV-Power}$ are 0.35 redder than the mean values of β_{UV-SED} for the same population of galaxies.

hand, we use the best-fit SED to obtain the $\beta_{UV-Power}$ associated with the power-law method. In that case, we are working with a simulated spectrum and its associated SED, then, if both methods are consistent we should obtain similar β_{UV} . Figure A.1 shows the β_{UV} comparison, in green, when the both β_{UV} have been calculated from the same best-fit model, using the associated spectrum and SED. We can see that both methods are consistent as the differences, even if systematic, are within the uncertainty showed in Section 3.2 ($\Delta\beta_{UV} \sim 0.2$).

We perform an additional test, where we include uncertainty at each photometric data point of the SED. We add a Gaussian scatter to the derived best-fit SED and recompute the $\beta_{UV-Power}$. The scatter has been defined as equal to the observational photometric error for each band and LBG from our sample. Figure A.1 illustrates the comparison between the β_{UV-SED} and the $\beta_{UV-Power}$ derived from the best-fit model SED + scatter in blue. That shows a similar trend than that obtained when we compared the both β_{UV} in our LBG sample. This suggests that the differences between the two methods are basically due to the scatter in the photometric data points as a consequence of the photometric uncertainty. Koprowski et al. (2018) also found similar discrepancies and suggested that these inconsistencies are driven by scatter in measured values of β_{UV} from limited photometry that serves to flatten IRX- β_{UV} relation artificially. These authors obtained that the scatter is significantly reduced by determining β_{UV} from SED-fitting analysis.

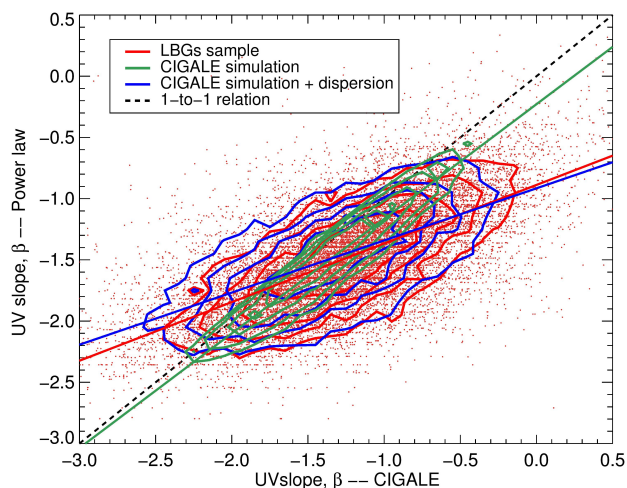


Fig. A.1: Comparison between the β_{UV} derived from the SED-fitting analysis and the power-law fit method. Red corresponds to the derived β_{UV} from the real data. Green represents the first simulation, where the two methods are compared using the β_{UV} derived best-fit spectrum and the associated SED. Blue shows the second simulation, where the two methods are compared using the β_{UV} derived best-fit spectrum and the associated SED + scatter. Continuum color lines illustrate the linear regression for each comparative. The dashed black line is the 1-to-1 relation.

If the SED-fitting analysis provides a good model fit to the photometric data points, why would the results from the two methods be different? We perform a simulation to try to understand the origin of that differences. We perform the SED-fitting analysis over the full LBG sample to derive their best-fit spectrum and SED (photometric data points of the best-fit model). On the one hand, we use the best-fit spectrum to calculate the β_{UV-SED} associated with the SED-fitting method. On the other

Appendix B: Fluxes and uncertainties at optical and NIR wavelengths for the 30 stacked LBGs SEDs at z 3

Stacking results at optical/NIR wavelength									
ID	S_B [μJy]	S_V [μJy]	S_r [μJy]	S_i [μJy]	S_z [μJy]	S_Y [μJy]	S_J [μJy]	S_H [μJy]	S_{K_s} [μJy]
LBG-L1	0.119±0.006	0.235±0.012	0.257±0.014	0.259±0.014	0.262±0.014	0.258±0.014	0.292±0.016	0.485±0.027	0.676±0.038
LBG-L2	0.223±0.012	0.416±0.022	0.477±0.026	0.520±0.029	0.496±0.027	0.536±0.030	0.604±0.034	0.943±0.053	1.260±0.071
LBG-L3	0.404±0.022	0.739±0.041	0.866±0.048	0.975±0.055	0.929±0.051	1.043±0.059	1.133±0.067	1.707±0.098	2.177±0.125
LBG-L4	0.732±0.050	1.313±0.078	1.554±0.094	1.822±0.107	1.690±0.099	1.841±0.113	2.027±0.129	2.886±0.187	3.603±0.230
LBG-M1	0.178±0.010	0.347±0.019	0.399±0.022	0.437±0.024	0.418±0.023	0.438±0.025	0.487±0.028	0.740±0.042	1.004±0.056
LBG-M2	0.202±0.011	0.398±0.022	0.471±0.026	0.510±0.030	0.517±0.029	0.579±0.034	0.684±0.040	1.126±0.065	1.503±0.087
LBG-M3	0.238±0.015	0.467±0.028	0.558±0.034	0.626±0.040	0.644±0.039	0.743±0.048	0.950±0.060	1.689±0.102	2.258±0.136
LBG-M4	0.247±0.020	0.472±0.032	0.573±0.039	0.669±0.047	0.650±0.044	0.828±0.064	1.073±0.075	2.132±0.140	2.970±0.187
LBG-M5	0.268±0.027	0.538±0.049	0.625±0.054	0.738±0.064	0.700±0.057	0.854±0.097	1.234±0.108	2.804±0.229	4.220±0.334
LBG-M6	0.175±0.035	0.399±0.059	0.527±0.094	0.650±0.109	0.601±0.073	0.670±0.200	1.218±0.154	3.066±0.393	5.251±0.515
LBG- β_1	0.191±0.010	0.356±0.019	0.409±0.022	0.445±0.025	0.442±0.024	0.470±0.026	0.532±0.030	0.815±0.045	1.057±0.059
LBG- β_2	0.149±0.008	0.309±0.017	0.366±0.020	0.389±0.023	0.454±0.026	0.561±0.033	0.680±0.042	1.130±0.067	1.476±0.087
LBG- β_3	0.096±0.007	0.235±0.015	0.277±0.018	0.349±0.023	0.382±0.024	0.537±0.042	0.672±0.054	1.149±0.089	1.527±0.111
LBG- β_4	0.079±0.009	0.214±0.020	0.271±0.025	0.391±0.042	0.402±0.038	0.538±0.075	0.756±0.099	1.513±0.184	2.304±0.291
LBG-M β_1 -M $_0\beta_0$	0.213±0.012	0.408±0.022	0.480±0.026	0.534±0.030	0.524±0.029	0.576±0.033	0.675±0.038	1.077±0.061	1.399±0.078
LBG-M β_1 -M $_0\beta_1$	0.140±0.008	0.303±0.017	0.366±0.021	0.409±0.025	0.465±0.027	0.597±0.038	0.754±0.047	1.248±0.076	1.609±0.097
LBG-M β_1 -M $_0\beta_2$	0.096±0.009	0.223±0.018	0.278±0.022	0.368±0.033	0.384±0.029	0.477±0.052	0.654±0.068	1.137±0.109	1.464±0.143
LBG-M β_1 -M $_1\beta_0$	0.331±0.032	0.598±0.050	0.729±0.066	0.860±0.077	0.786±0.069	0.812±0.092	1.237±0.115	2.654±0.244	4.012±0.311
LBG-M β_1 -M $_1\beta_1$	0.187±0.022	0.391±0.037	0.463±0.045	0.548±0.050	0.572±0.047	0.836±0.089	1.118±0.107	2.594±0.223	3.761±0.293
LBG-M β_1 -M $_1\beta_2$	0.098±0.014	0.271±0.039	0.364±0.047	0.446±0.054	0.512±0.057	0.764±0.119	1.188±0.154	2.708±0.302	4.560±0.495
LBG-M β_2 -M $_0\beta_0$	0.187±0.010	0.361±0.020	0.422±0.023	0.465±0.026	0.465±0.026	0.508±0.029	0.586±0.034	0.900±0.051	1.143±0.064
LBG-M β_2 -M $_0\beta_1$	0.080±0.006	0.205±0.014	0.237±0.015	0.317±0.020	0.321±0.022	0.450±0.044	0.535±0.055	0.753±0.069	0.997±0.085
LBG-M β_2 -M $_1\beta_0$	0.254±0.015	0.490±0.028	0.587±0.034	0.653±0.040	0.665±0.039	0.774±0.047	0.957±0.058	1.620±0.097	2.169±0.127
LBG-M β_2 -M $_1\beta_1$	0.126±0.010	0.279±0.019	0.344±0.024	0.418±0.028	0.472±0.031	0.620±0.055	0.782±0.060	1.391±0.101	1.743±0.127
LBG-M β_2 -M $_2\beta_0$	0.275±0.024	0.520±0.038	0.623±0.045	0.712±0.052	0.691±0.051	0.835±0.071	1.108±0.085	2.175±0.156	2.908±0.197
LBG-M β_2 -M $_2\beta_1$	0.133±0.015	0.299±0.030	0.392±0.037	0.504±0.057	0.536±0.044	0.780±0.090	1.104±0.101	2.227±0.172	3.205±0.252
LBG-M β_2 -M $_3\beta_0$	0.325±0.036	0.607±0.055	0.708±0.066	0.844±0.077	0.800±0.074	0.896±0.112	1.262±0.136	2.968±0.283	4.326±0.361
LBG-M β_2 -M $_3\beta_1$	0.129±0.022	0.311±0.048	0.385±0.055	0.455±0.059	0.464±0.051	0.710±0.137	1.141±0.150	2.453±0.272	3.594±0.364
LBG-M β_2 -M $_4\beta_0$	0.242±0.063	0.420±0.087	0.628±0.171	0.783±0.201	0.634±0.114	0.553±0.158	1.073±0.183	2.585±0.571	4.714±0.745
LBG-M β_2 -M $_4\beta_1$	0.117±0.027	0.398±0.079	0.441±0.082	0.530±0.084	0.602±0.083	1.013±0.150	1.441±0.220	3.511±0.450	5.601±0.591

Appendix C: Fluxes and uncertainties at FIR and MIR wavelength for the 30 stacked LBGs SEDs at z 3. It also includes the stacking analysis performed for AzTEC (1.1mm), and previously presented in AM16.

ID	Stacking results at MIR/FIR/millimeter wavelengths										
	$S_{3.6\mu\text{m}}$ [μJy]	$S_{4.5\mu\text{m}}$ [μJy]	$S_{5.8\mu\text{m}}$ [μJy]	$S_{8\mu\text{m}}$ [μJy]	$S_{24\mu\text{m}}$ [μJy]	$S_{100\mu\text{m}}$ [mJy]	$S_{160\mu\text{m}}$ [mJy]	$S_{250\mu\text{m}}$ [mJy]	$S_{350\mu\text{m}}$ [mJy]	$S_{500\mu\text{m}}$ [mJy]	$S_{1.1\text{m}}$ [mJy]
LBG-L1	0.997±0.061	1.218±0.066	1.273±0.096	1.442±0.143	11.41±1.36	0.092±0.034	0.296±0.079	0.569±0.151	0.517±0.167	0.391±0.163
LBG-L2	1.670±0.102	1.787±0.098	1.880±0.134	1.697±0.183	12.05±1.53	0.140±0.039	0.289±0.097	0.663±0.177	0.786±0.203	0.768±0.201
LBG-L3	2.410±0.164	2.744±0.160	2.614±0.228	2.743±0.378	19.01±2.67	0.141±0.055	0.311±0.138	0.773±0.264	0.970±0.309	0.650±0.302
LBG-L4	4.167±0.442	4.649±0.408	5.610±0.578	5.878±0.837	26.52±6.29	<0.432>	0.450±0.332	1.442±0.703	1.704±0.828	1.966±0.825
LBG-M1	1.217±0.078	1.280±0.071	0.934±0.107	0.754±0.165	10.12±1.46	<0.102>	0.280±0.092	0.497±0.164	0.544±0.183	0.551±0.181
LBG-M2	1.847±0.126	2.224±0.126	2.794±0.205	2.241±0.314	21.74±2.73	0.198±0.058	0.548±0.152	1.355±0.268	1.390±0.288	1.001±0.268	0.194 ± 0.093
LBG-M3	3.560±0.242	4.096±0.234	4.913±0.340	4.192±0.529	40.59±5.11	0.269±0.072	0.977±0.199	2.157±0.402	2.307±0.450	1.902±0.415	0.313 ± 0.143
LBG-M4	6.095±0.429	7.268±0.443	8.076±0.565	7.698±0.807	60.16±7.89	0.417±0.130	1.089±0.326	2.944±0.652	3.359±0.708	2.446±0.637	0.407 ± 0.209
LBG-M5	8.546±0.695	10.49±0.66	12.89±0.90	14.86±1.36	98.71±13.2	0.533±0.168	2.196±0.428	5.527±1.075	6.675±1.192	6.267±1.113	1.196 ± 0.415
LBG-M6	15.16±1.50	18.47±1.64	23.54±2.05	25.46±2.76	185.1±29.8	0.992±0.258	3.325±0.872	10.91±2.39	12.13±2.57	9.732±2.216	2.045 ± 0.916
LBG- β 1	1.282±0.075	1.388±0.074	1.160±0.090	1.159±0.133	8.511±1.13	0.054±0.022	0.092±0.047	0.246±0.102	0.400±0.123	0.559±0.134
LBG- β 2	2.159±0.145	2.588±0.151	2.629±0.204	2.706±0.326	24.33±3.08	0.195±0.051	0.709±0.139	1.424±0.262	1.326±0.273	0.986±0.249
LBG- β 3	3.017±0.304	3.869±0.320	4.550±0.427	3.759±0.758	43.77±6.09	0.252±0.111	1.316±0.327	3.527±0.628	3.402±0.638	2.724±0.576
LBG- β 4	5.439±0.963	6.575±0.848	7.102±1.227	9.409±1.747	75.74±14.2	0.691±0.231	1.465±0.566	3.779±1.112	3.271±1.079	1.376±0.846
LBG-M β 1-M β 0	1.820±0.108	2.006±0.107	2.063±0.137	1.722±0.184	15.36±1.86	0.112±0.032	0.380±0.087	0.744±0.159	0.733±0.178	0.690±0.177
LBG-M β 1-M β 1	2.448±0.187	3.016±0.183	3.172±0.262	2.841±0.483	30.06±3.79	0.223±0.068	0.782±0.199	2.126±0.389	2.231±0.410	1.697±0.368
LBG-M β 1-M β 2	2.725±0.490	3.312±0.413	4.460±0.653	2.845±1.278	46.41±8.43	0.237±0.188	1.133±0.485	2.987±0.866	2.654±0.831	1.618±0.736
LBG-M β 1-M β 0	8.931±0.703	11.01±0.77	13.72±1.07	16.08±1.56	108.7±15.5	0.615±0.213	2.556±0.538	6.193±1.264	7.361±1.378	5.983±1.214
LBG-M β 1-M β 1	8.272±0.686	9.699±0.667	12.73±1.01	10.56±1.27	091.5±14.0	0.372±0.148	1.644±0.527	4.847±1.151	5.538±1.309	4.677±1.252
LBG-M β 1-M β 2	12.27±1.87	15.44±1.96	16.64±2.06	19.99±3.06	124.5±26.0	0.823±0.325	1.734±0.767	5.817±1.939	6.203±2.330	5.006±1.693
LBG-M β 2-M β 0	1.401±0.088	1.499±0.081	1.331±0.118	1.046±0.168	10.91±1.53	0.076±0.032	0.242±0.090	0.559±0.157	0.553±0.174	0.460±0.173
LBG-M β 2-M β 1	1.623±0.308	2.007±0.217	2.237±0.450	1.955±0.947	30.04±5.69	<0.432>	0.968±0.385	1.851±0.647	1.902±0.666	1.533±0.595
LBG-M β 2-M β 0	2.962±0.193	3.481±0.195	4.210±0.281	3.678±0.430	30.31±3.78	0.204±0.059	0.850±0.166	1.550±0.314	1.564±0.356	1.372±0.344
LBG-M β 2-M β 1	3.344±0.368	3.903±0.324	4.454±0.522	3.632±0.922	38.24±6.38	0.308±0.132	0.941±0.372	2.964±0.751	2.847±0.751	2.500±0.716
LBG-M β 2-M β 0	5.965±0.463	7.005±0.439	7.737±0.600	7.520±0.931	60.01±8.39	0.374±0.146	1.282±0.401	3.441±0.773	3.993±0.866	2.986±0.765
LBG-M β 2-M β 1	6.688±0.719	8.004±0.681	9.259±0.875	8.350±1.167	66.27±12.0	0.500±0.211	<1.548>	2.158±1.095	2.335±1.209	1.466±0.940
LBG-M β 2-M β 0	8.844±0.751	10.42±0.69	12.64±1.03	15.80±1.52	102.0±14.8	0.666±0.211	2.173±0.527	5.536±1.408	6.356±1.434	6.292±1.327
LBG-M β 2-M β 1	8.095±1.110	10.45±1.01	13.14±1.24	13.19±2.21	82.31±15.2	<0.759>	1.951±0.652	5.790±1.412	7.513±1.735	6.588±1.607
LBG-M β 2-M β 0	15.15±1.73	18.23±1.85	24.68±2.65	25.79±4.07	189.2±40.1	0.968±0.346	2.445±0.996	10.36±2.39	12.16±2.93	10.38±3.00
LBG-M β 2-M β 1	15.23±2.29	19.23±2.55	23.59±2.77	27.00±3.48	195.9±37.4	0.984±0.343	4.434±1.276	11.75±3.69	12.48±4.06	8.879±3.043

Appendix D: Physical parameters derived by SED-fitting analysis for the 30 stacked LBGs SEDs at $z \approx 3$

ID	τ [Myr]	Age [Myr]	SFR [$M_{\odot}\text{yr}^{-1}$]	$\log(M_{*}) [M_{\odot}]$	E(B-V)	A_{FUV}	δ	β_{UV}	$\log(L_{\text{FUV}} [L_{\odot}])$	U_{min}	γ	$\log(L_{\text{IR}} [L_{\odot}])$	$\log(M_{\text{dust}} [M_{\odot}])$
Stacking as a function of L_{FUV} (LBG-L)													
LBG-L1	147 ± 334	132 ± 89	20.6 ± 6.6	9.58 ± 0.11	0.29 ± 0.03	2.33 ± 0.14	0.18 ± 0.09	-1.76 ± 0.19	10.40 ± 0.03	38.5 ± 10.9	0.032 ± 0.011	11.38 ± 0.05	7.55 ± 0.26
LBG-L2	271 ± 439	157 ± 96	33.6 ± 5.3	9.61 ± 0.10	0.18 ± 0.02	2.00 ± 0.10	-0.08 ± 0.07	-1.56 ± 0.19	10.66 ± 0.024	28.5 ± 13.9	0.028 ± 0.012	11.48 ± 0.04	7.92 ± 0.52
LBG-L3	369 ± 488	179 ± 104	48.6 ± 9.3	9.76 ± 0.10	0.12 ± 0.02	1.71 ± 0.14	-0.23 ± 0.09	-1.47 ± 0.19	10.92 ± 0.03	31.1 ± 13.7	0.033 ± 0.011	11.59 ± 0.06	7.97 ± 0.58
LBG-L4	180 ± 368	143 ± 99	68.5 ± 21.4	10.06 ± 0.11	0.13 ± 0.03	1.59 ± 0.15	-0.15 ± 0.14	-1.47 ± 0.19	11.17 ± 0.03	19.2 ± 15.6	0.024 ± 0.013	11.80 ± 0.08	8.79 ± 0.72
Stacking as a function of β_{UV} (LBG- β)													
LBG- β 1	443 ± 513	229 ± 118	21.0 ± 4.3	9.49 ± 0.09	0.12 ± 0.02	1.64 ± 0.13	-0.22 ± 0.10	-1.52 ± 0.19	10.60 ± 0.03	5.7 ± 7.2	0.034 ± 0.010	11.23 ± 0.06	8.62 ± 0.43
LBG- β 2	405 ± 495	159 ± 94	63.6 ± 9.5	9.75 ± 0.13	0.24 ± 0.03	2.87 ± 0.14	-0.10 ± 0.10	-1.01 ± 0.20	10.54 ± 0.03	41.1 ± 9.3	0.029 ± 0.012	11.76 ± 0.04	7.89 ± 0.13
LBG- β 3	250 ± 420	110 ± 53	115 ± 12	9.97 ± 0.08	0.37 ± 0.02	3.83 ± 0.19	-0.02 ± 0.04	-0.67 ± 0.22	10.43 ± 0.03	35.2 ± 10.9	0.014 ± 0.007	12.06 ± 0.03	8.34 ± 0.19
LBG- β 4	279 ± 450	216 ± 180	118 ± 48	10.42 ± 0.18	0.40 \AA ± 0.05	4.11 ± 0.28	-0.001 ± 0.095	-0.46 ± 0.26	10.42 ± 0.03	41.6 ± 9.5	0.036 ± 0.009	12.18 ± 0.08	8.28 ± 0.17
Stacking as a function of stellar mass (LBG-M)													
LBG-M1	465 ± 514	112 ± 48	29.6 ± 3.4	9.23 ± 0.10	0.13 ± 0.02	1.89 ± 0.10	-0.28 ± 0.07	-1.60 ± 0.19	10.59 ± 0.03	30.9 ± 14.2	0.026 ± 0.013	11.33 ± 0.04	7.77 ± 0.68
LBG-M2	404 ± 494	122 ± 54	64.2 ± 7.4	9.64 ± 0.10	0.22 ± 0.02	2.61 ± 0.13	-0.09 ± 0.04	-1.36 ± 0.19	10.65 ± 0.03	36.9 ± 10.6	0.026 ± 0.012	11.74 ± 0.03	7.94 ± 0.16
LBG-M3	484 ± 520	249 ± 112	88.1 ± 10.3	10.12 ± 0.10	0.28 ± 0.02	2.84 ± 0.14	0.01 ± 0.05	-1.17 ± 0.20	10.72 ± 0.03	35.2 ± 10.7	0.025 ± 0.012	11.95 ± 0.03	8.18 ± 0.16
LBG-M4	344 ± 461	382 ± 251	99.8 ± 27.1	10.54 ± 0.11	0.35 ± 0.04	3.13 ± 0.21	0.10 ± 0.09	-1.04 ± 0.21	10.73 ± 0.03	33.0 ± 11.1	0.029 ± 0.012	12.10 ± 0.06	8.35 ± 0.17
LBG-M5	443 ± 525	414 ± 270	182 ± 58	10.81 ± 0.11	0.44 ± 0.04	3.67 ± 0.21	0.16 ± 0.08	-1.08 ± 0.24	10.78 ± 0.03	24.8 ± 9.6	0.017 ± 0.009	12.39 ± 0.05	8.82 ± 0.18
LBG-M6	444 ± 523	612 ± 451	257 ± 95	11.22 ± 0.10	0.55 ± 0.05	4.44 ± 0.25	0.18 ± 0.07	-0.75 ± 0.33	10.66 ± 0.04	25.7 ± 10.5	0.018 ± 0.009	12.62 ± 0.05	9.04 ± 0.20
Stacking as a function of (β_{UV}, M_{*}) - LBG-M β 1													
LBG-M β 1- $M_0\beta_0$	422 ± 502	200 ± 106	37.9 ± 5.9	9.66 ± 0.10	0.17 ± 0.02	2.08 ± 0.12	-0.12 ± 0.08	-1.40 ± 0.19	10.66 ± 0.03	36.2 ± 11.6	0.031 ± 0.011	11.52 ± 0.05	7.73 ± 0.24
LBG-M β 1- $M_0\beta_1$	413 ± 497	117 ± 45	89.4 ± 8.9	9.77 ± 0.09	0.27 ± 0.02	3.19 ± 0.16	-0.10 ± 0.03	-0.87 ± 0.20	10.54 ± 0.03	35.3 ± 10.9	0.018 ± 0.009	11.90 ± 0.03	8.16 ± 0.19
LBG-M β 1- $M_0\beta_2$	346 ± 475	104 ± 57	114 ± 20	9.87 ± 0.15	0.34 ± 0.03	3.77 ± 0.19	-0.05 ± 0.06	-0.70 ± 0.23	10.43 ± 0.03	37.3 ± 11.59	0.024 ± 0.012	12.02 ± 0.05	8.25 ± 0.31
LBG-M β 1- $M_1\beta_0$	368 ± 487	428 ± 308	171 ± 66	10.91 ± 0.11	0.48 ± 0.04	3.53 ± 0.20	0.25 ± 0.08	-1.26 ± 0.23	10.83 ± 0.03	31.8 ± 11.4	0.019 ± 0.009	12.42 ± 0.06	8.73 ± 0.23
LBG-M β 1- $M_1\beta_1$	580 ± 558	473 ± 273	159 ± 36	10.71 ± 0.11	0.39 ± 0.03	3.78 ± 0.19	0.05 ± 0.07	-0.73 ± 0.25	10.64 ± 0.03	27.1 ± 12.3	0.017 ± 0.009	12.29 ± 0.05	8.75 ± 0.35
LBG-M β 1- $M_1\beta_2$	308 ± 472	457 ± 390	132 ± 65	11.00 ± 0.11	0.45 ± 0.04	4.23 ± 0.21	0.07 ± 0.10	-0.23 ± 0.31	10.51 ± 0.04	27.7 ± 13.7	0.029 ± 0.012	12.39 ± 0.04	8.85 ± 0.56
Stacking as a function of (β_{UV}, M_{*}) - LBG-M β 2													
LBG-M β 2- $M_0\beta_0$	377 ± 490	148 ± 69	28.8 ± 3.3	9.42 ± 0.07	0.13 ± 0.01	1.89 ± 0.09	-0.29 ± 0.04	-1.42 ± 0.19	10.60 ± 0.02	33.7 ± 12.9	0.028 ± 0.011	11.35 ± 0.03	7.67 ± 0.48
LBG-M β 2- $M_0\beta_1$	237 ± 410	92 ± 47	61.4 ± 17.5	9.61 ± 0.11	0.28 ± 0.04	3.26 ± 0.20	-0.09 ± 0.07	-0.78 ± 0.22	10.37 ± 0.03	29.3 ± 14.9	0.024 ± 0.012	11.75 ± 0.08	8.28 ± 0.75
LBG-M β 2- $M_1\beta_0$	270 ± 440	155 ± 94	69.6 ± 13.5	9.95 ± 0.11	0.23 ± 0.02	2.58 ± 0.12	-0.06 ± 0.08	-1.21 ± 0.19	10.74 ± 0.03	38.5 ± 10.5	0.028 ± 0.012	11.84 ± 0.04	8.02 ± 0.18
LBG-M β 2- $M_1\beta_1$	329 ± 468	166 ± 107	93.6 ± 24.6	10.01 ± 0.15	0.31 ± 0.03	3.37 ± 0.20	-0.05 ± 0.07	-0.71 ± 0.21	10.52 ± 0.03	29.4 ± 13.7	0.021 ± 0.012	11.97 ± 0.08	8.41 ± 0.50
LBG-M β 2- $M_2\beta_0$	449 ± 521	351 ± 230	122 ± 31	10.49 ± 0.13	0.36 ± 0.04	3.18 ± 0.21	0.10 ± 0.08	-1.14 ± 0.22	10.77 ± 0.03	32.3 ± 12.2	0.022 ± 0.011	12.16 ± 0.06	8.47 ± 0.27
LBG-M β 2- $M_2\beta_1$	343 ± 481	401 ± 320	91.9 ± 33.4	10.56 ± 0.10	0.33 ± 0.04	3.48 ± 0.26	-0.04 ± 0.09	-0.42 ± 0.25	10.56 ± 0.03	37.1 ± 12.6	0.034 ± 0.001	12.09 ± 0.08	8.34 ± 0.66
LBG-M β 2- $M_3\beta_0$	378 ± 473	483 ± 304	155 ± 46	10.88 ± 0.07	0.44 ± 0.04	3.38 ± 0.17	0.22 ± 0.08	-1.19 ± 0.24	10.83 ± 0.03	25.7 ± 12.9	0.024 ± 0.012	12.35 ± 0.04	8.84 ± 0.41
LBG-M β 2- $M_3\beta_1$	463 ± 533	418 ± 286	175 ± 54	10.78 ± 0.13	0.45 ± 0.04	4.20 ± 0.21	0.07 ± 0.08	-0.51 ± 0.35	10.53 ± 0.04	23.3 ± 12.5	0.017 ± 0.009	12.37 ± 0.05	8.93 ± 0.39
LBG-M β 2- $M_4\beta_0$	555 ± 542	932 ± 571	235 ± 83	11.36 ± 0.11	0.58 ± 0.05	4.18 ± 0.26	0.27 ± 0.09	-1.01 ± 0.40	10.69 ± 0.06	18.9 ± 11.7	0.021 ± 0.011	12.60 ± 0.05	9.27 ± 0.43
LBG-M β 2- $M_4\beta_1$	407 ± 511	416 ± 296	303 ± 111	11.10 ± 0.13	0.50 ± 0.05	4.72 ± 0.23	0.06 ± 0.09	-0.28 ± 0.39	10.61 ± 0.05	33.5 ± 12.1	0.019 ± 0.010	12.65 ± 0.05	8.97 ± 0.35